Geophysical Journal International

Geophys. J. Int. (2021) **224,** 1477–1504
Advance Access publication 2020 October 12
GJI Seismology

doi: 10.1093/gji/ggaa487

On the wobbles of phase-velocity dispersion curves

Petr Kolínský, Götz Bokelmann and the AlpArray Working Group*

Department of Meteorology and Geophysics, University of Vienna, UZA II, Althanstraße 14, 1090 *Vienna, Austria. E-mail: petr.kolinsky@univie.ac.at*

Accepted 2020 October 7. Received 2020 September 9; in original form 2020 May 20

SUMMARY

To calculate phase-velocity dispersion curves, we introduce a method which reflects both structural and dynamic effects of wave propagation and interference. Rayleigh-wave fundamental-mode surface waves from the South Atlantic Ocean earthquake of 19 August 2016, $M = 7.4$, observed at the AlpArray network in Europe are strongly influenced by the upper-mantle low-velocity zone under the Cameroon Volcanic Line in Central Africa. Predicting phase-delay times affected by diffraction from this heterogeneity for each station gives phase velocities as they would be determined using the classical two-station method as well as the advanced array-beamforming method. Synthetics from these two methods are thus compared with measurements. We show how the dynamic phase velocity differs from the structural phase velocity, how these differences evolve in space and how two-station and array measurements are affected. In principle, arrays are affected with the same uncertainty as the two-station measurements. The dynamic effects can be several times larger than the error caused by the unknown arrival angle in case of the two-station method. The non-planarity of the waves and its relation to the arrival angle and dynamic phase-velocity deviations is discussed. Our study is complemented by extensive review of literature related to the surface wave phase-velocity measurement of the last 120 years.

Key words: Structure of the Earth; Surface waves and free oscillations; Wave propagation; Wave scattering and diffraction.

1 INTRODUCTION

Much (if not most) of our knowledge about the Earth`s uppermost mantle comes from analysing seismic surface waves, through the study of frequency-dependent (group or phase) velocities, the so-called 'dispersion curves'. In certain cases, like for the oceanic lithosphere (e.g. James *et al.* 2014), the phase-velocity dispersion curve of Rayleigh waves can have a local minimum. Indeed, theory predicts that dispersion curves must always be smooth, with velocity generally increasing with period, and having at most a single minimum spanning a broad range from 30 to 70 s. From now on, we will call these expected smooth and monotonic dispersion curves as 'simple curves'. Observations are somewhat in contrast with simple curves predicted by theory though. Using either tripartite (Evernden 1954) or two-station method (Brune & Dorman 1963), the measured dispersion curves show non-random deviations. Pilant & Knopoff (1964) already noted that if two or more wave trains interfere, not only the amplitude shows beats, but also the phases are affected by 'fluctuations'. Knopoff *et al.* (1966) noted that these phase irregularities made it almost impossible to determine Earth structure from the observation. In the Appendix, we give an extensive overview of the papers dealing with surface wave measurements. Problems with determining accurate phase velocities were experienced already in the advent of dispersion-curve studies. All the authors recognized that the undulated measurements could not be explained by structural models. Some of the authors already excluded the measurement errors as a cause. From now on, we will denote these observed oscillations (scatter, fluctuations, irregularities, disturbances, undulations, perturbations, changes in derivative) as dispersion curve wobbles. More precisely, a wobbled dispersion curve is not following the trend of a simple curve and the wobbles can be attributed neither to the structure nor to measurement errors.

Wobbles have usually their maxima and minima separated by 10–20 s in the period range from 5 to 200 s. There has been suspicion early-on that such increases and decreases of phase velocity can hardly be explained by structural models, for example from the sensitivities calculated by Brune & Dorman (1963), Fig. 14; Novotný (1970), Figs 1–10 and Novotný *et al.* (2005), Fig. 2. Sensitivities are plotted as partial derivatives of phase velocity with respect to shear-wave velocity (*P*-wave velocity, density) for each depth separately over the period range. It shows that every layer influences a very broad range of periods. It is impossible to construct a layer with parameters influencing only a narrow period band to cause

* www.alparray.ethz.ch

increase/decrease of phase velocity in only this band. Also note that nowadays these sensitivities are usually plotted in a different way (Smith *et al.* 2004; Lebedev *et al.* 2013): each line represents sensitivity for a given period depending on depth (while before each line represented sensitivity for given depth over the period range). The contemporary way of representing the sensitivities shows the same: for each period, the sensitivity is non-zero over such a broad range of depths that we cannot construct a layer which would decrease (increase) the velocity in a small range (∼10–20 s) of periods. Wobbled dispersion curves are also unlikely to be associated with any particular measurement method. For details, see the Appendix.

Many papers show phase-velocity dispersion curves, which are smooth and simple (monotonic, no wobbles). There are three reasons for the curves to be simple. (i) Phase-velocity dispersion curves calculated from a structural model are always simple (see the Appendix for examples of the large number of references that show such theoretical dispersion curves). (ii) There are measured curves which look quite simple, especially for long propagation paths of thousands of kilometres (see Kolínský *et al.* (2011) for shorter paths on the other hand). (iii) The last category of simple dispersion curves relates again to curves, which are 'observed', however, these are dispersion curves representing not a single pure-path measurement, as above, but rather a region or locality. Such dispersion curves can be obtained by averaging or merging the pure-path curves, like in Baumont *et al.* (2002). Generally, such regionalized curves are found in all tomographic studies (see the Appendix), where the phase-velocity maps are used to compile 'local' dispersion curves characterizing the structure at the given node of the tomography grid.

Since the first observations, seismologists have tried to present an explanation for the discrepancy between simple modelled and wobbled observed curves. Brune & Dorman (1963) attributed the scatter to the interference of Sa and Sn waves with the fundamental modes of surface waves. Pilant & Knopoff (1964) described fluctuations based on interference from multiple events and signals arriving over multiple paths. Knopoff & Mal (1967) showed how the back reflection from inclined Moho produces phase shifts. They successfully modelled a wobbled dispersion. Thatcher & Brune (1969) discussed the mode interference as a possible cause of anomalous apparent phase velocities of Love waves. Since then, the possible explanations repeat regularly in other papers, see the Appendix. Detailed investigation was given by Weidner (1972, 1974): the observed wobbles are attributed to interference caused by mutually delayed parts of the fundamental mode of Rayleigh waves scattered from the Mid Atlantic Ridge. This explanation is very close to what we suggest.

Together with the attempts of explanation, researchers tried to remove the wobbles. Noponen (1966) used smoothing of the phase-velocity wobbles and Dean (1986) suggested simultaneous smoothing of phase and group curves. Other attempts include averaging of individual measurement from the two-station method (e.g. Darbyshire *et al.* 2004), two-plane wave fit to the observed wavefield (Forsyth & Li 2005) and selection of only the smooth portions of dispersion curves (Polat *et al.* 2012; Soomro *et al.* 2016). One aspect to note here is that all these methods of removing the wobbles are independent of the cause of the wobbles - averaging and smoothing removes the wobbles without asking, why they are there. Even though the two-plane wave approach is capable to fit the complex wavefield better than a single-plane wave, it still does not explain, why the wavefield is so complex.

It has been repeatedly assumed that array techniques (beamforming) are capable of determining the phase velocity better than the two-station method because they simultaneously search for both the magnitude of the velocity as well as its direction, see Widmer-Schnidrig & Laske (2007) and references therein. It is true that knowing the arrival angle of incoming waves removes the bias caused by unknown direction of propagation as in the case of the two-station method. However, significant wobbles remain in the array-based dispersion curves (Kolínský *et al.* 2014 and references in the Appendix) showing that the non-plane wavefield causes significantly more serious problem than the unknown arrival angle. Although the effects of incoming wavefield can be partially suppressed by averaging over many measurements from earthquakes in different backazimuths similarly like in the case of the two-station method, still array-based phase velocities are in principle affected by the non-structural wobbles. Barros *et al.* (2008) showed that smaller arrays produce higher wobbles than bigger arrays. We will later see that this effect corresponds to the two-station method also yielding higher wobbles on shorter interstation paths.

We will show two-station and array phase-velocity measurements in our paper. Thanks to the large AlpArray project, we will show how the results vary in space observing surface waves propagating from a single earthquake, rather than how the results differ while observing various earthquakes at one locality as done by most of the referenced studies. This will allow us to generalize some of the previous conclusions and to propose a model, which explains the dispersion-curve wobbles obtained both from the two-station method as well as from the array beamforming. We will model the wave propagation yielding synthetic dispersion curves for both methods. The comparison of our observation and modelling preserves the dispersion-curve complexity for various lengths of the two-station profiles, for various positions of profiles and arrays in different distances from the earthquake source as well as it explains the variation in space laterally to the wave propagation direction. We will not only give a general explanation of possible causes of the wobbles, but we will locate the cause and predict the wobbles. This may lead to a qualitatively new method of removing the bias in the phase-velocity measurement, which is based on the knowledge of the cause of the bias (that is not the focus of this paper though).

The modelling is based on the conclusions drawn by Kolínský *et al.* (2020), referenced as 'KSB2020' from now on. We have shown therein that when propagating from the South Atlantic Ocean to Europe, the wavefield is diffracted from a distant heterogeneity so that the arrival angles differ significantly from the great circle paths. Moreover, the arrival angles form a stripe-like pattern, which is connected to the wavefield and not the local structure, as shown by Kolínský & Bokelmann (2019) (referenced as 'KB2019' from now on), where similar patterns were observed for 20 earthquakes from different azimuths. These arrival angles are directly connected to similar stripe-like pattern of phase-time delays. In our paper, we will show, how these stripes of alternating positive and negative phase-time delays translate into the wobbles of dispersion curves.

The left-hand side of Fig. 1 shows a reprint of Fig. 4 from Noponen (1966), who studied propagation of surface waves from earthquakes in Greece through the Baltic Shield by the two-station method. In the right-hand panel of Fig. 1, his NUR-OUL profile (black line) for event 1 is redrawn together with a profile of similar length using the current AlpArray stations (blue line). In addition, the red line shows a modelled wobbled dispersion curve using the technique proposed in our paper.

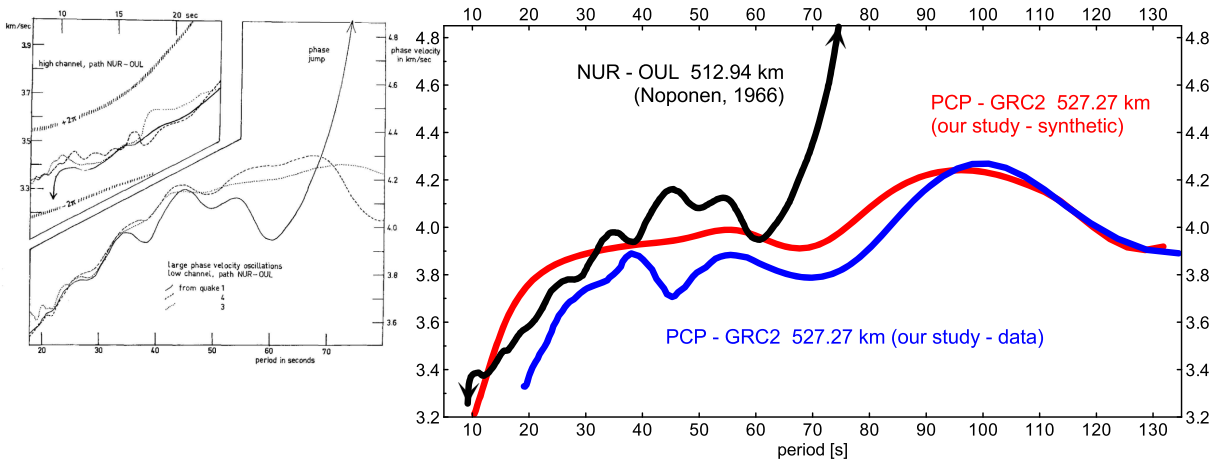

Figure 1. Examples of wobbled phase-velocity dispersion curves. Left-hand panel: reprint of Fig. 4 from Noponen (1966) showing two-station NUR-OUL profile of 512.94 km length crossing the Baltic Shield, using Rayleigh waves propagating from three earthquakes in Greece. Right-hand panel: the dispersion curve from Noponen (1966) for the event 1 is shown by black line. Blue line shows a two-station measurement using the profile PCP—GRC2 (527.27 km) crossing the Alps, for Rayleigh waves propagating from the earthquake in the South Atlantic Ocean. Red curve shows the synthetic modelled dispersion for the same profile using the Cameroon Volcanic Line model from KSB2020. The axes of both panels have the same scale.

2 MEASUREMENT

2.1 Two-station method

The dispersion-curve measurement between two stations is based on the technique developed and described by Kolínský *et al.* (2011). First, the fundamental mode is isolated using multiple-filtering (usually around 100 filters) in the frequency domain and tapering in the time domain (Kolínský & Brokešová 2007). Envelope maxima (group velocity) are picked starting from the longest waves proceeding continuously to shorter waves. We are able to pick the fundamental mode wavegroup even for periods, where other wavegroups have larger amplitudes. This allows us to exploit a broad period range of surface waves. Fundamental mode wavegroup is tapered using a time window of a 4-period length. Filtering and tapering is the same for all records. As a result, we have a set of quasi-harmonic signals filtered in the frequency-time domain for each station, see Fig. 4 in Kolínský *et al.* (2011) and Fig. 2 in KB2019.

The phase-velocity measurement is then accomplished in the time domain. Filtered and tapered quasi-harmonic signals of the same period recorded by two stations are cross-correlated. Times of the cross-correlation function maxima give us a set of possible dispersion curves differing by generally unknown number of cycles between the stations. Because the station distances are only up to several wavelengths of the longest waves, the proper dispersion branch is selected using an approximate guess of the phase velocities for the waves around the period of 100 s. Other branches have unreasonably high or low velocities. Following again the continuous branch towards shorter periods, we can select the proper branch for the short periods as well.

2.2 Array beamforming

Array processing follows the procedure developed in Kolínský *et al.* (2014) and later used by KB2019. The data handling is basically the same as for the two-station method. We use exactly the same sets of filtered and tapered fundamental mode wavegroups as in the case of the two-station method. The only difference is that we now cross-correlate not the pairs of quasi-monochromatic signals for two stations along a profile, but rather neighboring stations grouped around a central station. Such a group of stations forms a subarray, in our case of a diameter of 160 km. We obtain a time delay for each neighbouring station with respect to the central one. Having the geometry and time delays, the slowness vector is determined by linear regression assuming a plane wave propagation across the subarray. There is no issue with unknown number of wave cycles because the aperture of the array is small compared to the wavelength and only one of the dispersion branches gives phase velocity in the expected range.

Every station of the network can turn into a central station of such a subarray. We look for neighboring stations in the range of distances from 20 to 80 km from the central station, and if there are at least five such neighbouring stations, the phase-velocity beamforming is provided. The average number of stations in a subarray is 13.1 for the selected earthquake (see the next Section 3 - Data and also Tab. 1 in KB2019). The latter paper also gives details about the data quality assessment, time-residual analysis for each subarray and each period and other details. The records of the selected earthquake have been already processed in KB2019 and KSB2020. Here, we follow exactly the same procedure, just the period range is broader now.

3 DATA

To demonstrate the surface wave dispersion measurements, we selected a shallow (10 km) earthquake, which occurred under the Southern Atlantic Ocean on 19 August 2016. Its magnitude was $M = 7.4$. It is one of the 20 earthquakes investigated by KB2019, see Tab. 1 and Fig. 11 therein and one of the two used to reveal the structure of the Cameroon Volcanic Line (CVL) used in KSB2020. Records of the vertical component of the AlpArray broadband seismic network (Fuchs *et al.* 2015, 2016; Hetényi *et al.* 2018) are used together with permanent seismic stations in Europe, see yellow triangles in Fig. 2 framed by the magenta line. The region includes both the Alpine area as well as the Apennine Peninsula. After careful manual data quality check, we further removed three stations with respect to what has been used by KB2019 and KSB2020 keeping 534 stations in total for the processing. Out of these, 499 stations were used as central stations of local subarrays (compare it with

502 subarrays in the latter papers). The distance of the earthquake epicentre to the centre of the AlpArray region is approximately 12 000 km. Rayleigh waves propagating from this earthquake to Europe show significant stripe-like pattern caused by the diffraction after passing the low-velocity region under the CVL in Central Africa (KSB2020) and the magnitude is big enough to yield high signal-to-noise ratio across the whole AlpArray network over a broad period range from 15 to 180 s. In our current paper, we show a reprocessed array-based arrival-angle measurements similar to KB2019 and KSB2020 as well as new two-station measurements prepared solely for the purpose of this paper. Note that the period range used in our current paper is much broader than what has been used both by KB2019 and KSB2020.

4 MODELLING

The goal of the modelling is to calculate phase-velocity dispersion curves, which take into account the wave interference of diffracted waves after passing a distant small-scale scatterer. The approach we propose differs significantly from calculating dispersion curves in a given structural model taking into account only the structure. We, in addition, consider also the finite-frequency wave-propagation effects, which allow us to model dynamic phase-velocity dispersion curves. We are then able to show, how much this dynamic phase velocity differs from the structural phase velocity, which would be the one if only the structural model is considered (Wielandt 1993).

We follow the procedure suggested by KB2019 and used by KSB2020, based on the theory of Nolet & Dahlen (2000). We use Gaussian beams to predict the phase-time delay τ of surface waves perturbed by a velocity anomaly. The anomaly placed in a homogeneous space produces Gaussian-shaped initial time delay (as defined by Nolet & Dahlen 2000). The anomaly and the homogeneous space around it represent a 2-D model. This 2-D model is different for each period T. The velocity of the medium around the anomaly as well as the properties of the anomaly, vary with period T (and hence with depth) allowing us to consider a 3-D structural model of the medium. The wavefield is calculated for the region after passing the anomaly, where the medium is purely 1-D. Properties of the perturbed wavefield at selected period are given by three parameters: the half-width of the anomaly $L(T)$ (the anomaly is represented by a box-car in our approach, with a half-width equal to the half-width of the Gaussian-shaped initial time delay), the initial time delay $\tau_{\max}(T)$ of the wave right after passing the anomaly and the phase velocity $c(T)$ of the surrounding medium. Having these three parameters set, we can predict the phase-time delays $\tau(x,R,T)$ (and arrival-angle deviations) for any point (x,R) after the anomaly. The meaning of x and R follows the notation given by Nolet & Dahlen (2000) and it is the same as used in KB2019 and KSB2020. The map projection in Fig. 3 keeps the great circle paths parallel to each other (green and orange lines are the same as in Fig. 2). Distance x is measured from the anomaly along the great circles from the epicentre. Lines of constant x are hence following the great circle wavefronts, and they are represented as straight red lines plotted for every 1000 km from the anomaly. Distance R is the lateral distance measured perpendicularly to x shown by brown lines also for every 1000 km to both sides from the orange axis of symmetry ($R = 0$) of the diffraction pattern. Note that while the red lines of constant x follow the great circle wavefronts, the brown lines of constant R do not follow the great circle paths as the mutual distance between any two great circle paths varies, while the distance between the brown lines is constant. The phase-time delays are calculated for any period T as

$$\tau(x,\,R,\,T) = \frac{T}{2\pi}\arctan\left[\frac{\mathrm{Im}(1+Q)}{\mathrm{Re}(1+Q)}\right], \tag{1}$$

where

$$Q = \frac{e^{i\frac{2\pi}{T}\tau_{\max}(T)} - 1}{\sqrt{\frac{ixc_{\mathrm{glb}}(T)T}{\pi L^2(T)} + 1}} \cdot \exp\left[-\frac{\left({}^{R}\!/_{L(T)}\right)^2}{1 + \frac{ixc_{\mathrm{glb}}(T)T}{\pi L^2(T)}}\right]. \tag{2}$$

The equations for calculating the phase-time delay are rewritten from Eqs 2 and 3 in KB2019 with only substituting for $\lambda = cT$ and $\omega = 2\pi/T$ (see also Eqs 2 and 3 in KSB2020). We set $L(T)$, $\tau_{\max}(T)$ and $c_{\mathrm{glb}}(T)$, we decide for a point (x,R) and we directly get the phase-time delay at this point for given period T in a 1-D medium with $c_{\mathrm{glb}}(T)$. To obtain the arrival-angle deviations, we use Eq. 4 from KB2019 (also Eq. 1 in KSB2020). It gives the arrival-angle deviation $A(x,R,T)$ as a lateral derivative (along R-axis) of the phase-time delay $\tau(x,R,T)$ as

$$A(x,\,R,\,T) = \arctan\left[c_{\mathrm{loc}}(T)\frac{\mathrm{d}\tau(x,\,R,\,T)}{\mathrm{d}R}\right]. \tag{3}$$

There is a small difference in notation of the phase velocity c (c_{glb} and c_{loc}) with respect to the same equations in KB2019 and KSB2020. This will be discussed later. This modelling was used by KSB2020 for revealing the anomaly, which causes the stripe-like interference pattern for Rayleigh waves propagating from two South Atlantic Ocean earthquakes across Central Africa to Europe. This low-velocity anomaly was identified as the Cameroon Volcanic Line placed partially beneath the continent and partially beneath the ocean.

For the purposes of forward modelling in our current study, we directly use the parameters of the anomaly determined by KSB2020. The anomaly head is at the location 10.5°N/15.0°E, see Fig. 2, map on the left-hand side. Green line represents great circle connecting the epicentre of the $M = 7.4$ earthquake and the centre of the AlpArray region. Orange line is the great circle connecting the epicentre and the anomaly head representing the symmetry axis of the diffraction pattern. Modelled arrival-angle deviations caused by the anomaly at this location with parameters obtained by the inversion in KSB2020 for 100 s surface wave [full width $2\times L(100\text{ s}) = 350$ km; $\tau_{\max}(100\text{ s}) = 66$ s; $c(100\text{ s}) = 4.08$ km s^{-1}] are shown by transparent colour pattern over the map in Fig. 2. The results for $2\times L(T)$ and $\tau_{\max}(T)$ of KSB2020 are replotted in the right-hand side of Fig. 2 (black lines representing the 13 possible anomaly locations and blue line representing the final best-fitting spot).

For the purposes of the current study, we extended the model of the anomaly for the period range 10–200 s, while KSB2020 gave the results only for the range 50–120 s. The extrapolation of the results both to shorter and longer periods is given by magenta dots for both $2\times L(T)$ and $\tau_{\max}(T)$ in Fig. 2. Every single dot represents a period for which we provide the modelling. In the range from 10 to 200 s, we set 121 discrete periods with geometrically increasing steps between them to resemble the dispersion-curve measurement using the multiple-filtering technique. Setting the time delay of the anomaly to $\tau_{\max} = 1$ s for periods shorter than $T = 36$ s means that the anomaly is effectively non-existent for shorter waves. Narrowing the anomaly for longer periods effectively diminishes the effect of the scattering even though we keep the same time delay of $\tau_{\max} = 80$ s for waves above $T = 114$ s. For the surrounding medium, we use the phase velocity calculated for the PREM (Dziewonski & Anderson 1981). For the details, see KSB2020. Note that this extrapolation is used here solely for the purposes of the forward modelling

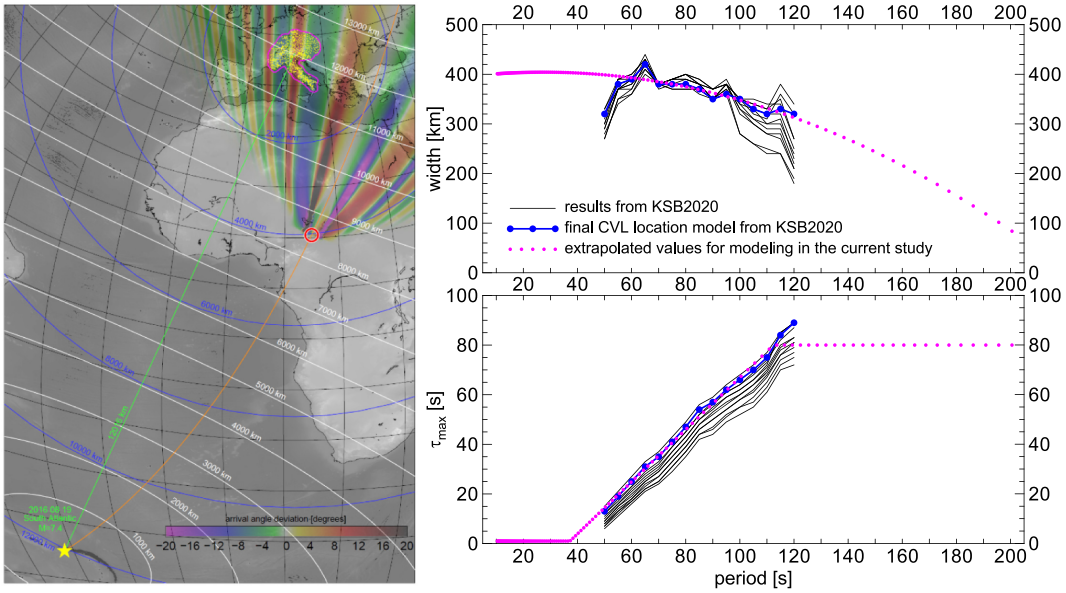

Figure 2. Overview of the model. Left-hand map: epicentre location as well as 534 stations used in this study are shown. Final location of the Cameroon Volcanic Line anomaly head from KSB2020 is depicted by red circle. Arrival-angle deviation pattern predicted by the modelling is shown for 100 s surface wave. Great circle between epicentre and the centre of the AlpArray region (green) as well as great circle corresponding to the axis of symmetry of the pattern (orange) are drawn. Right-hand panels: Widths and initial time delays obtained by the inversion for 13 possible anomaly head locations (thin black lines) and for the final location (blue) from KSB2020. Magenta dots represent the values extrapolated for the modelling in the current study (121 discrete periods).

of the synthetic dynamic phase-velocity dispersion curves, and in no case it should propose any additional structural features under the Cameroon Volcanic Line. Also note that the only heterogeneity in our structural model takes place under the CVL exclusively. Everywhere else, the structure is only 1-D (PREM). Meaning, also under the AlpArray network, the structural model is solely 1-D. As discussed already in KSB2020 (see section 6.1 therein), in reality, the CVL is not the only heterogeneity on the way from the South Atlantic Ocean to Europe. Measurement at shorter periods show clear stripes of arrival-angle deviations pointing in another direction, see Fig. 3 in KSB2020. The goal of our study is to show, how a single anomaly affects the dispersion curve measurement. We do not intend to explain all the peculiarities observed in the data. The CVL was identified as by far the strongest anomaly on the way and this is why we use it to demonstrate the principle of how the wobbles affect the dispersion curves.

We use the modelling in three ways:

(i) *Fine maps*. Phase-time delays and arrival-angle deviations are modelled at a very fine grid of locations (x,R) in a global scale ($0.1^\circ \times 0.1^\circ$). This allows us to plot smooth diffraction patterns over large areas like in Fig. 2. Actual results of such a modelling are given for five selected periods in Fig. 4. We see arrival-angle deviations plotted as colour maps. The plot is the same in the background of all four columns of Fig. 4. In the first column ('data meas'), this fine model is compared with the arrival-angle measurements on the real data plotted using the same colour scale inside the magenta-bordered AlpArray region. The same has been plotted also by KSB2020, see the left-hand column of Fig. 3 therein (the selected periods differ).

(ii) *Direct modelling*. Here we calculate the phase-time delays only for the locations of stations. To be able to predict the phase velocity and arrival angles, we also need to calculate the phase-time delays in the immediate vicinity of the station to determine the spatial derivatives of the phase-time delay distribution. The derivative in the lateral direction R gives us the arrival angle. The inverse of the derivative in the radial direction x, corrected for the arrival angle, gives us the phase velocity. To obtain robust results by spatial differentiating, we use the phase-time delays calculated for points in a distance of ± 10 km before (and after) as well as ± 10 km to both sides from the station to determine the values at the location of the station. This roughly corresponds to the $\pm 0.1^\circ$ grid on which the derivatives were calculated in case of the fine modelling above. Note that the station distance of the AlpArray project is around 40 km (Heténi *et al.* 2018). An example of arrival-angle deviations modelled using this approach is given inside the magenta-bordered AlpArray region in the second column ('direct modelling') of Fig. 4 (with the fine model in the background). This comparison shows us, how well our station distribution maps the stripe-like pattern spatially. Phase velocities obtained using the direct modelling will be discussed later.

(iii) *Measurement on synthetics*. In this case, we again predict the phase-time delays for the locations of stations. No additional derivatives are needed. These phase-time delays are then treated, as if they were measured between pairs of stations. It applies both for the two-station measurement as well as for the array beamforming. We simply subtract the phase-time delays at the two stations and we add the time corresponding to the propagation in the 1D PREM structure beneath the network. Hence, we obtain the time difference exactly as if it was measured by correlating the two quasi-harmonic signals. In case of the two-station method, the difference of epicentral distances divided by this time difference gives us directly the phase-velocity dispersion curve. In case of the array beamforming, all the time differences between the neighbouring stations and the central station of each subarray are again passed through the linear regression to determine the slowness vector (the absolute value of the phase velocity as well as the direction of propagation). An example of such an array measurement on synthetic phase-time delays is given in the third column ('synthetics meas') of Fig. 4 (again with the fine model in the background). Such a comparison shows us how

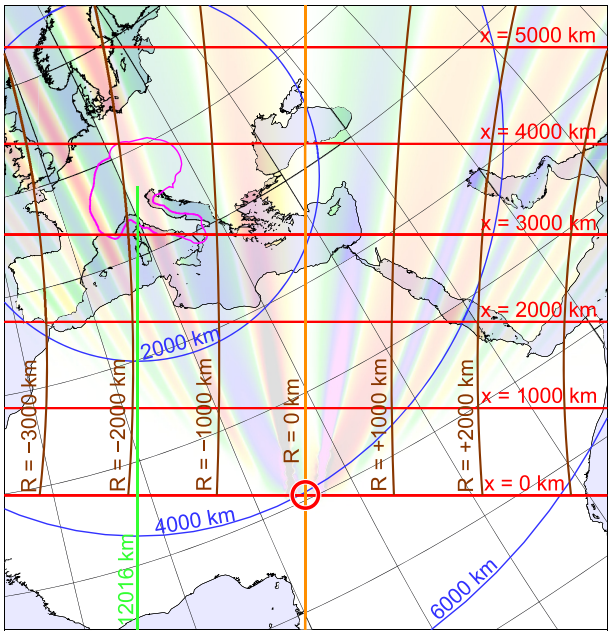

Figure 3. Coordinate system of x and R shown as a grid by every 1000 km. The magenta AlpArray region, light green great circle connecting the epicentre and the centre of the AlpArray, orange great circle connecting the epicentre and the anomaly head, blue circles showing the distance from the centre of the AlpArray and the diffraction pattern are the same as in Fig. 2. The map projection is chosen so that the great circles are represented by mutually parallel vertical lines while the great circle wavefronts form mutually parallel horizontal lines.

well our station distribution together with the array-beamforming method maps the arrival-angle pattern. Again, the phase velocities obtained by this array measurement on synthetics will be discussed later.

The fourth column ('time delay') of Fig. 4 shows the phase-time delays (inside the AlpArray region, brown-orange colour scale) calculated by the fine modelling (i) with again the arrival-angle deviations in the background. This comparison shows the relation between the two quantities. We see that arrival-angle deviations have their maxima and minima (the darkest colours) at the places where the phase-time delays are zero (white stripes inside the AlpArray region, the time delays have their highest lateral derivative there) and, the opposite, the zero (white) stripes of the arrival-angle deviations are found at the places where the phase-time delays are maximal or minimal (and hence their derivative is zero).

5 RESULTS

5.1 Emergence of phase-velocity wobbles

First, we explain how the stripe-like diffraction pattern of interfering waves translates into dispersion-curve wobbles. We consider two two-station profiles: one is between stations A188A and A213A of a length of 343.38 km shown by red lines in Fig. 5, the other between stations A291A and A076A of a length of 372.97 km shown by blue lines. Both profiles are well-aligned with the great-circle direction: the difference of the backazimuths between the more distant station and epicentre, and more distant station and the closer station are 0.4° and 1.5° for red and blue profiles, respectively. Nine maps in the middle of Fig. 5 show exactly the same phase-time delays using the same colour scale as in the fourth column in Fig. 4 (where only every second period is shown). Now, in Fig. 5, the pattern is plotted over the whole map. Black dots in both panels above and below the maps show the positions of these nine selected periods for which the maps are plotted (five of these periods are shown also in Fig. 4). Red and blue wobbled lines are the phase-velocity dispersion curves measured on synthetic phase-time delays (modelling (iii) above). When moving from short to long periods, the phase-time delay pattern 'opens' its shape - stripes are getting wider and are moving to the west (away from the axis of symmetry), see Fig. 4 here in our current paper and also Figs 12 and 13 in KB2019. Thus, the two stations at the given profiles are repeatedly affected by alternating stripes of positive and negative phase-time delays, which give rise to apparently higher or apparently lower phase velocities measured between the two stations. At period of 103 s, the red profile has its first station (closer to the epicentre) located in the brown region, meaning negative time delay. The wave is coming apparently earlier there. The second station is located in the orange region, where the time delay is positive and hence the wave comes apparently later to this station. Measuring the time difference between these two stations at that period gives us longer propagation time than would be the one if only the structure (PREM in our case) between the stations was considered. This results in apparently low phase velocity, which is why the black dot at 103 s period on the red curve lies well below the structural PREM phase velocity shown by light blue line. The same mechanism causes the positive velocity deviations as well, see for example the period of 139 s at the red curve.

Comparing the two dispersion curves (red and blue) we see that they differ in several ways. The red one has more wobbles - we see three positive and three negative extremes, while the blue one has only two positive and two negative wobbles. It is due to the fact that the stripes are getting narrower for the given period when moving laterally away from the axis of symmetry (to the west). Red profile is located more in this direction and hence when changing the period in the given range, more stripes of narrower width strike the stations with respect to the blue profile located more to the east, meaning closer to the axis of symmetry. As a consequence, the wobbles are also wider (in the period range sense) for the blue curve. In addition, the blue wobbles are also of lower amplitudes (less deviated from the structural PREM velocity). Even the phase-time delay stripes are of higher amplitude closer to the axis of symmetry, because they are wider, for the same profile length, it is less likely that one of the stations is struck by positive extreme and the other by the negative one at the same period. The stripes are simply too broad with respect to the profile length. Also, the stripes are more aligned to the great-circle paths around the axis of symmetry, meaning that it is again more likely that both stations are located in the same (positive/negative) stripe and so the wobbles are less pronounced. In the extreme case, if the two-station profile lies exactly at the axis of symmetry, meaning just behind the anomaly when looking from the epicentre, there would be no wobbles since both the stations will lie in the positive (central) stripe across the whole period range. This, however, does not mean that the dispersion curve would not be affected. It would still show a velocity different from the structural one, because even in the single (positive) delay time stripe, the delay changes with the distance from the anomaly. This is usually called 'wavefront healing'. Blue profile is also more distant in the radial direction from the anomaly than the red one. Later, we will see that the position of the profiles in the radial distance matters as well (it is not clearly seen yet from comparing only the two profiles in Fig. 5).

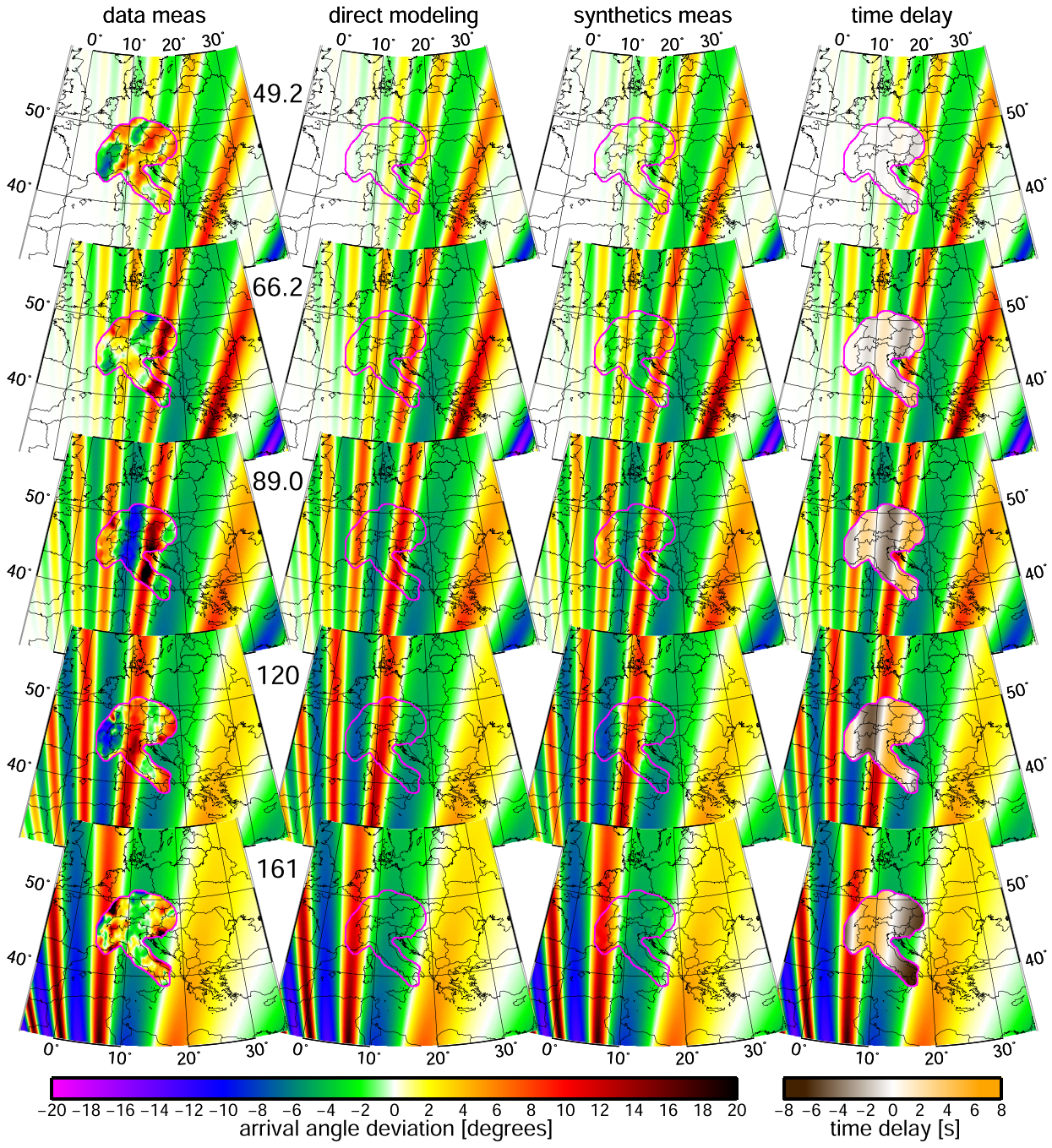

Figure 4. Measurement and modelling for five selected periods (rows). In the background of all four columns, we show the same arrival-angle deviations predicted on a fine grid over the global scale. Inside the magenta AlpArray region, the first column shows the measurement from KSB2020. The second column shows the direct modelling of the arrival angles. These are calculated by the same method as on the fine grid in the background, however, now only for the 499 subarray locations. Third column shows the arrival-angle deviations measured on synthetic phase-time delays. The last, fourth column shows the predicted phase-time delays. As the arrival angles are defined as a lateral derivative of these phase-time delays, we see that the zero (white stripes) regions of arrival angles correspond to the extremes of the phase-time delays and vice versa.

We again note that the structure under both (red and blue) profiles is the same, characterized by the light blue PREM phase-velocity dispersion curve in Fig. 5. Following the paper by Wielandt (1993), we denote this as 'structural' velocity. The wobbled dispersion curves are representing the phase velocities of the wavefield, and we call them 'dynamic' velocities, following again the terminology by Wielandt (1993). We can also note that below 40 s, where the CVL anomaly has disappeared in our modelling, the dynamic and structural velocities match each other (no diffraction and hence no interference takes place).

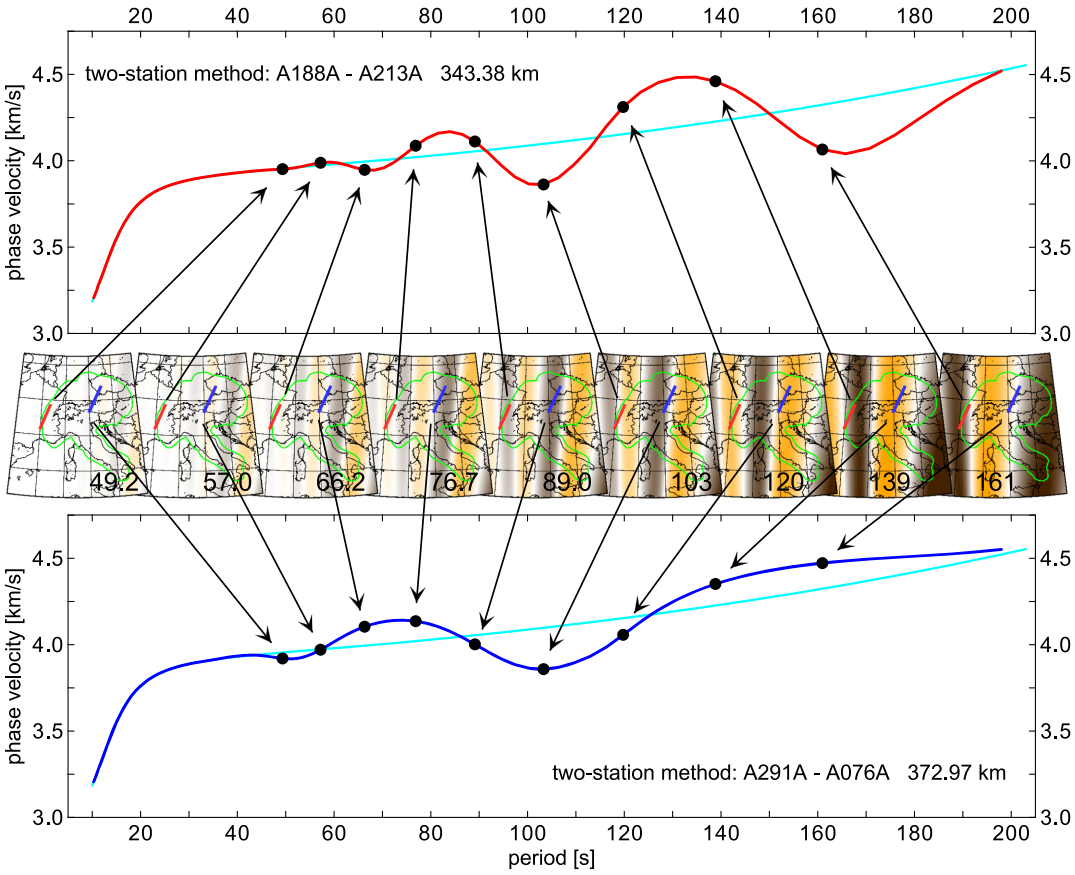

Figure 5. Synthetic dispersion curves for two two-station profiles in the AlpArray region (red and blue). The nine maps show the same phase-time delays as in Fig. 4 (right-hand column, only five of the nine periods are shown in Fig. 4). Velocities for these nine selected periods are depicted also over both the dispersion curves by black dots. Cyan lines are the PREM dispersions.

5.2 Two-station method

To see how the two-station measurements are affected spatially and to show how the synthetic model matches the observation, we used the AlpArray network to measure phase velocities over 95 profiles using both synthetic phase-time delays and real data. Profiles are organized in 5 sets of 19 profiles. They have three different lengths - we measured two sets of profiles of short distances, two sets of intermediate distances and one of long distances. Profiles in each set are located in similar radial distance from the anomaly (epicentre) and differ by the lateral position with respect to the axis of symmetry of the diffraction pattern. The geometry is given in Fig. 6. We take the advantage of the dense AlpArray seismic network, which allows us to select suitable two-station pairs of desired lengths and positions in the region. Dashed white lines show the great circles from the epicentre. Different sets of profiles are plotted by different colours.

Brown and orange sets are the shortest ones with average profile length of 144 km. The difference between these two sets is in the radial distance from the anomaly (epicentre) - the brown set is located much closer to the anomaly than the orange set. The average epicentral distance of the first stations of the 19 profiles in the brown set is 11 598 km while the average distance of the first stations in the orange set is 12 242 km. The mutual shift of the sets of 644 km represents 16 per cent of the distance (along x) to the CVL anomaly. Red and blue sets represent intermediate lengths with 361 km of profile length in average. Again, red set is closer to the epicentre than the blue one with 11 634 and 11 996 km average epicentral distances of the first stations in respective sets (difference of 362 km represents 9 per cent of the distance to the CVL anomaly). The longest green profiles have average length of 750 km. As they span almost the entire AlpArray region, there is no space for alternative positions for such long profiles. The lateral distance range of all five sets of profiles from the axis of symmetry of the diffraction pattern (along R) is 1000–2450 km. Many stations are repeatedly used in profiles of different sets.

Results of the measurement are given in Fig. 7. Each column of dispersion curves represents one set of profiles. Synthetic dispersion curves are plotted by respective colours (brown, orange, red, blue and green) as given in Fig. 6 and dispersion curves measured on real data are shown by grey lines. Profiles in each column are sorted by the distance from the axis of symmetry starting with the most distant profiles (west) at the top of the column ending up at the bottom with profiles located the closest to the axis of symmetry (east). Station names as well as the lengths of all profiles are given in the figure as well. In each plot, the structural PREM dispersion curve is given by light blue line. Below each of the five columns, all the 19 profiles are summarized together for the respective set.

Before we compare the synthetic and real measurements, we need to point out the principal difference between the two: while the real data obviously reflect the structure beneath the Alps, the synthetics do not. All the synthetic dispersion curves are calculated in 1-D PREM model, while the structure beneath the Alps is very heterogeneous. In addition, the CVL is not the only anomaly on the way from the South Atlantic Ocean to Europe. Real data measurements are affected by wobbles emerging from other scatterers elsewhere,

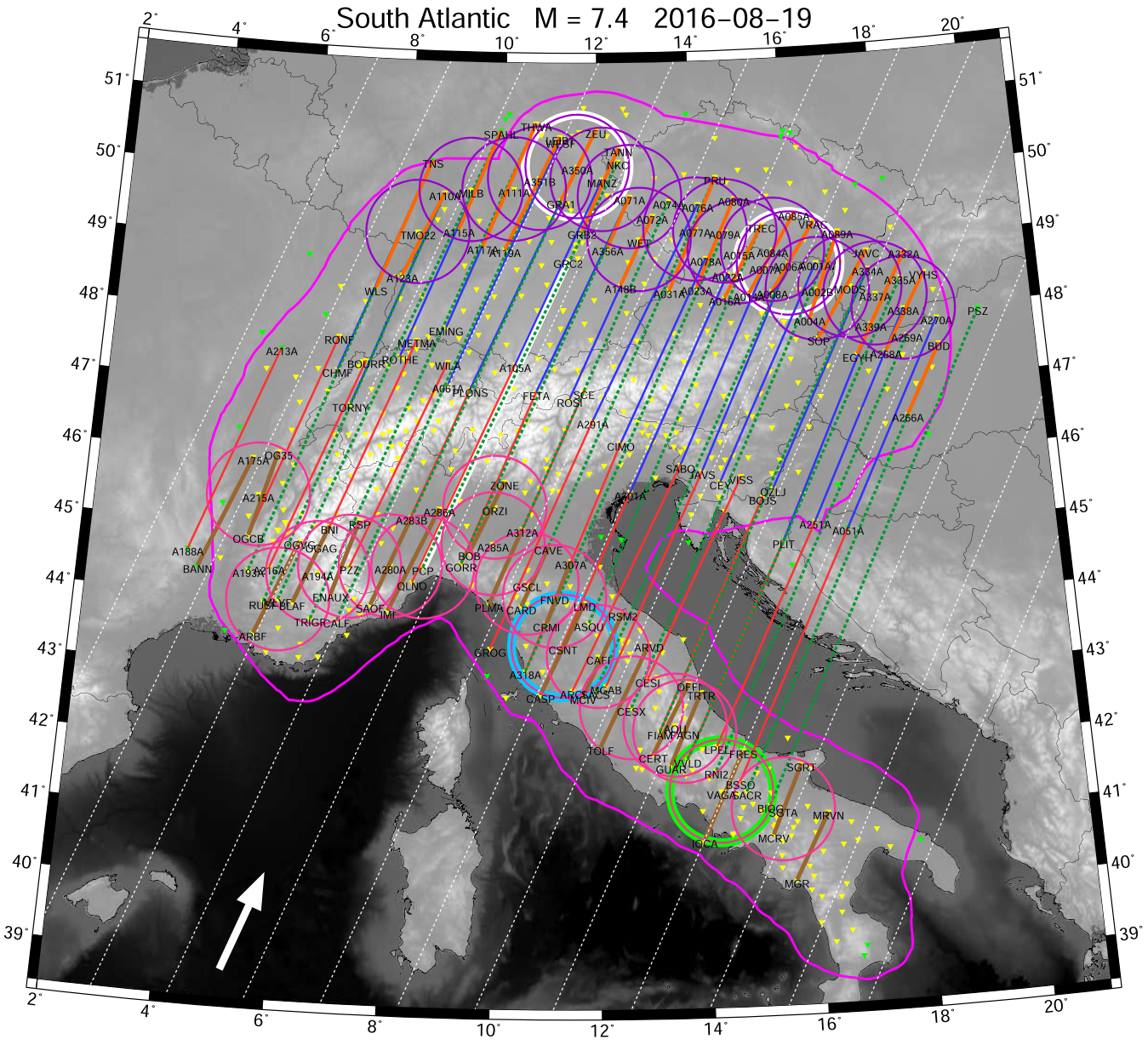

Figure 6. The AlpArray region with 534 stations (499 yellow triangles show the subarray central stations, 35 green triangles show the stations used as neighboring stations). By coloured lines, we show the two-station profiles, including the two shown in Fig. 5. Thick white profile PCP-GRC2 is used as an example in Fig. 1. Altogether, there are five sets of 19 profiles depicted by red, blue, green, brown and orange colours. In addition, there are also two sets of subarrays shown as pink and purple circles. Great circles from the earthquake are marked by dashed white lines. Arrow shows the direction of wave propagation. Arrays emphasized by white, light blue and light green circles are used for detailed examples, see the text.

see KSB2020 for the discussion. We are, however, interested in a qualitative comparison of the shapes of the curves in this moment to show, how the dynamic phase velocity adds up to the structural one. Looking at all the 95 plots in Fig. 7, we see that most of the dispersion curves show similar shapes comparing the synthetic and real ones. We may note that:

(i) Shorter profiles have bigger wobbles. This is best-seen in the bottom panels, where all the curves are plotted together. Going from left to right (brown to green set), we see that the range of velocities (wobbles) becomes smaller. This applies for both the synthetic as well as the real curves.

(ii) Profiles closer to the source (to the anomaly) have bigger wobbles. This is represented by the brown set having bigger wobbles than the orange set, and by the red set having bigger wobbles than the blue set. As the sets are sorted both by length and by distance to the anomaly, we see monotonically decreasing range of velocities (smaller wobbles) from brown (the shortest and also the closest) to green (the longest) profile.

(iii) Profiles more distant from the axis of symmetry have bigger wobbles. This can be seen by scrolling from the top profiles (west, the most distant) down to the bottom ones (east, the closest) dispersions. As we go east (closer to the axis of symmetry), the wobbles decrease. This applies for all five sets.

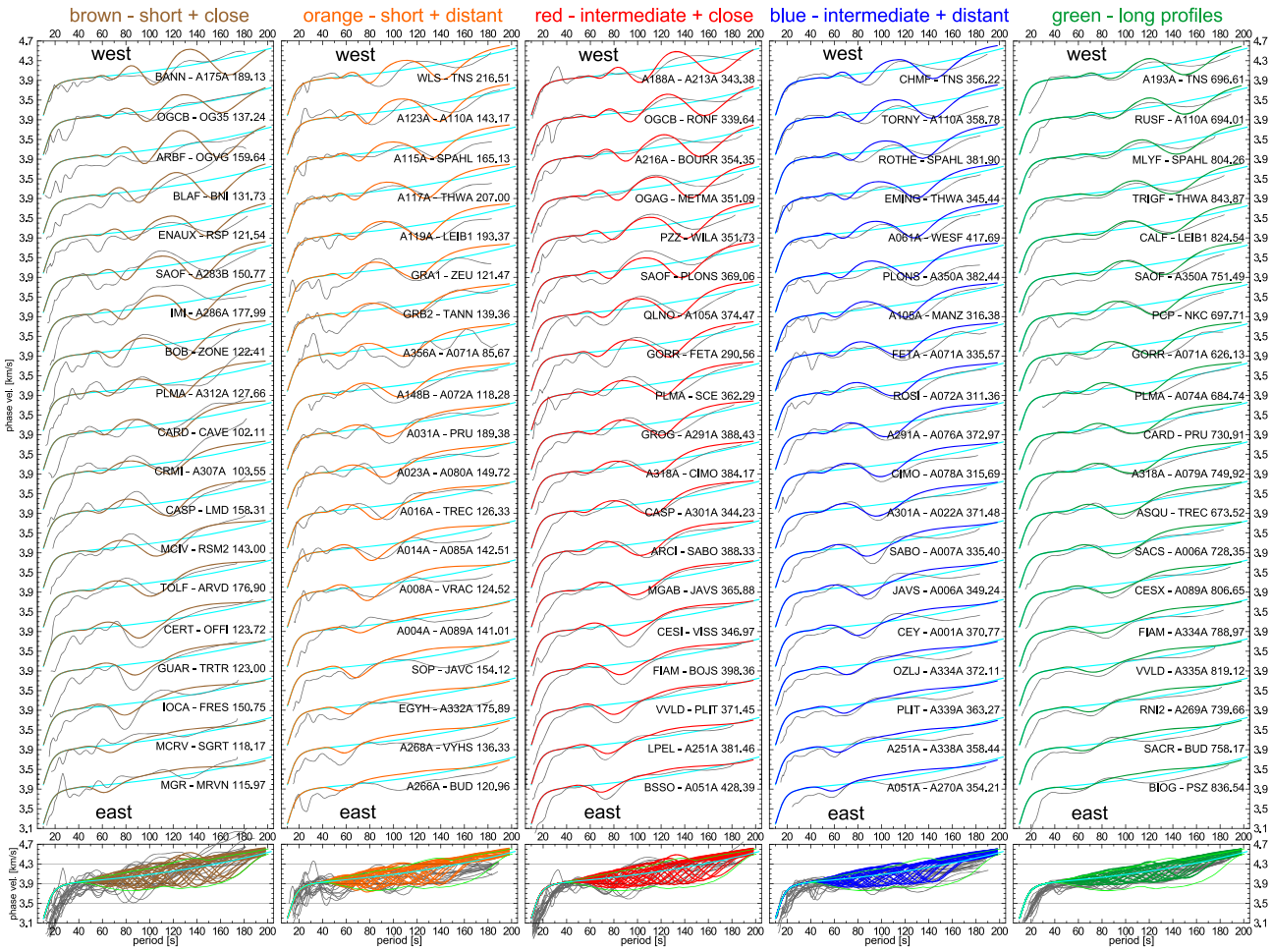

Figure 7. Five sets of two-station profiles. Synthetic dispersion curves are shown by colours corresponding to the profiles shown in Fig. 6. Brown and orange profiles are of the shortest lengths, red and blue profiles are of intermediate lengths and green profiles are the longest. The panel shows the western profiles on the top and the eastern at the bottom. Grey lines show the measured dispersions using the data from the earthquake. Bottom panels show all 19 curves merged into one panel to emphasize the range of velocities.

(iv) The match between synthetic and real curves is the better, the longer the profiles are.

(v) In each set, there is a pattern of wobbles, which is shifting to shorter periods when going from west (top) to east (bottom) curves. The maximum velocity at the brown profile BANN-A175A (top) around 135 s is slowly shifting to 45 s at MGR-MRVN profile (bottom), where it almost disappears. This applies for the following minimum as well going from 165 to 60 s. The same can be seen at all 5 sets. Synthetic dispersions show this wobble shift always very clearly. At the real data, the best pronounced shift of wobbles is revealed at both intermediate sets (red and blue). It is, however, present in all other real data sets as well.

(vi) Wobbles are more stretched along the period range for longer waves. Their minima and maxima are getting closer when we move to shorter periods.

(vii) The shorter the profiles are, the more complicated are the real dispersion curves at shorter periods. This property cannot be reflected in the synthetics, because below 40 s, the propagation is modelled as homogeneous (CVL anomaly disappears).

(viii) The real data have, in general, bigger wobbles than the synthetics. This behaviour is more pronounced for shorter profiles (brown, orange).

5.3 Array beamforming

We showed how the diffraction pattern influences the two-station measurement. Now, we will look at what happens when array beamforming is used for processing the same data. Fig. 8 has eight panels (a–h), each showing 499 curves (black lines) corresponding to all the subarrays used in our analysis. On the left-hand side, we show the arrival-angle deviations (a, c, e, g), on the right-hand side the phase-velocity dispersion curves (b, d, f, h). Each row (pair of panels) corresponds to different technique by which the curves were obtained.

The top pair (a, b) shows the subarray measurement on synthetic phase-time delays following the method '(iii) *Measurement on synthetics*' described above. No heterogeneity was considered anywhere in this case. It means that all the propagation was modelled as if the whole Earth was only 1-D PREM. The light blue lines show theoretical curves for the PREM, both for the velocities (b), as well as for the arrival-angle deviations (a), where the line is simply at zero (no deviations in 1-D model). The same light blue lines are plotted also in the other panels of Fig 8(c)–(h). The deviation of the 499 black lines from the light blue line in panels (a) and (b) shows, how well the array beamforming performs depending on the properties of the measurement, like subarray geometry, the technique used,

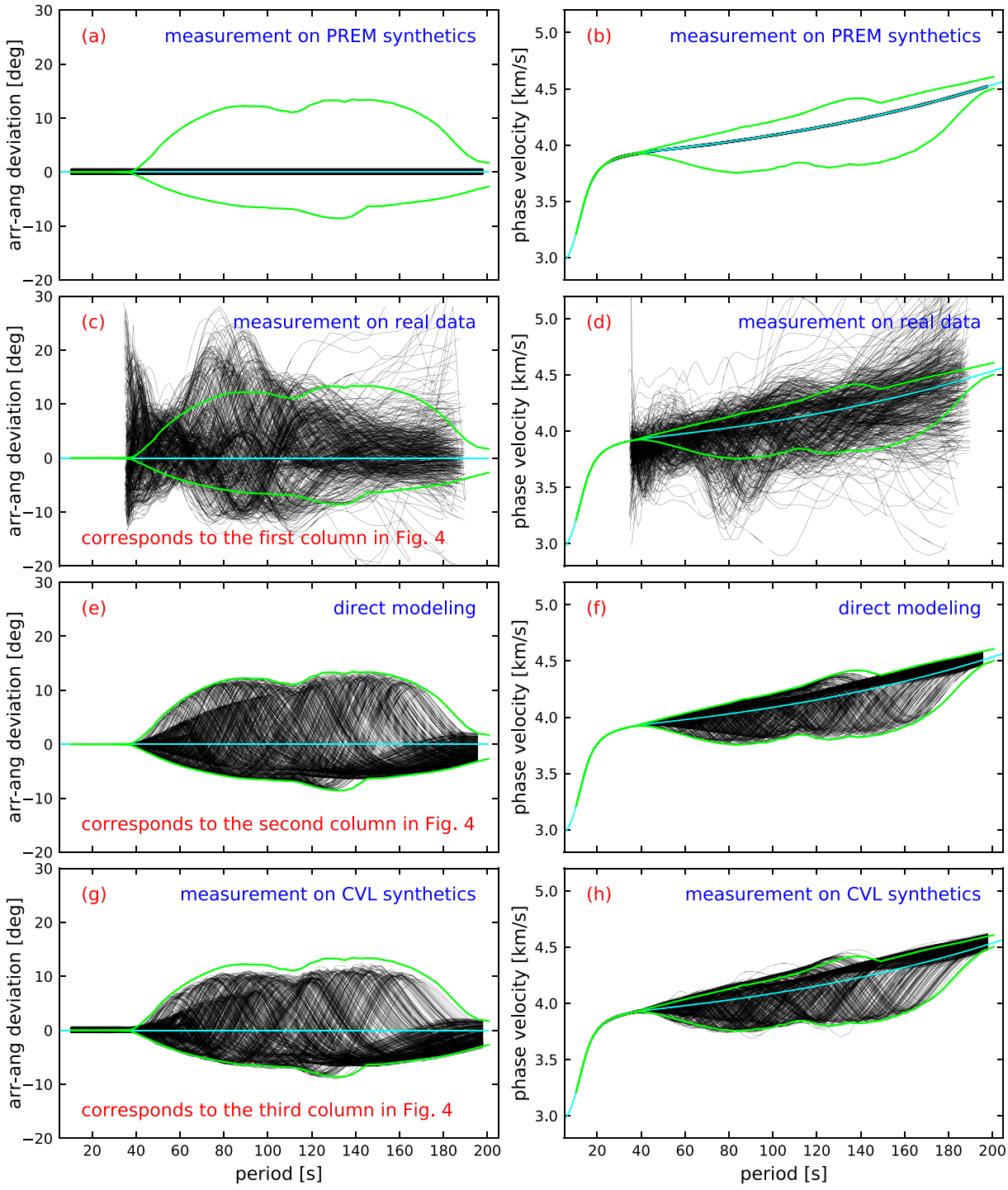

Figure 8. Arrival-angle deviations (left-hand column) and dispersion curves (right-hand column) for 499 subarrays of the AlpArray region. The upper panels show the results when the CVL anomaly was removed, meaning, all the propagation takes place only in the PREM. Arrival-angle deviations are expected to be zero, dispersion curves are expected to fit the PREM model. Second row is the measurement using data (corresponds to the 1st column in Fig. 4). Third row of panels shows the direct prediction of the arrival-angle deviations and dispersion curves using spatial derivatives around the station locations (corresponds to the 2nd column of Fig. 4). Ranges (envelopes) of these direct results are copied by green lines to all the other respective panels. The bottommost row of panels shows the measurement using the synthetic phase-time delays (corresponds to the 3rd column of Fig. 4).

sampling interval, number of stations in each subarray, epicentral distance (planarity of the waves) and so on. It gives us an idea about the precision of the technique itself, with arrival-angle deviations ranging between -0.52° and $+0.75^\circ$ (a) and phase velocities in the range of ± 0.019 km s^{-1} (b) around the PREM velocities. Such a deviation represents a measurement error of 0.48 per cent for the velocity of 4 km s^{-1}.

The second pair of panels (c, d) shows the results of measurement using the real data. We see a broad range of arrival-angle deviations (c) as well as of velocities (d). The distribution is however not

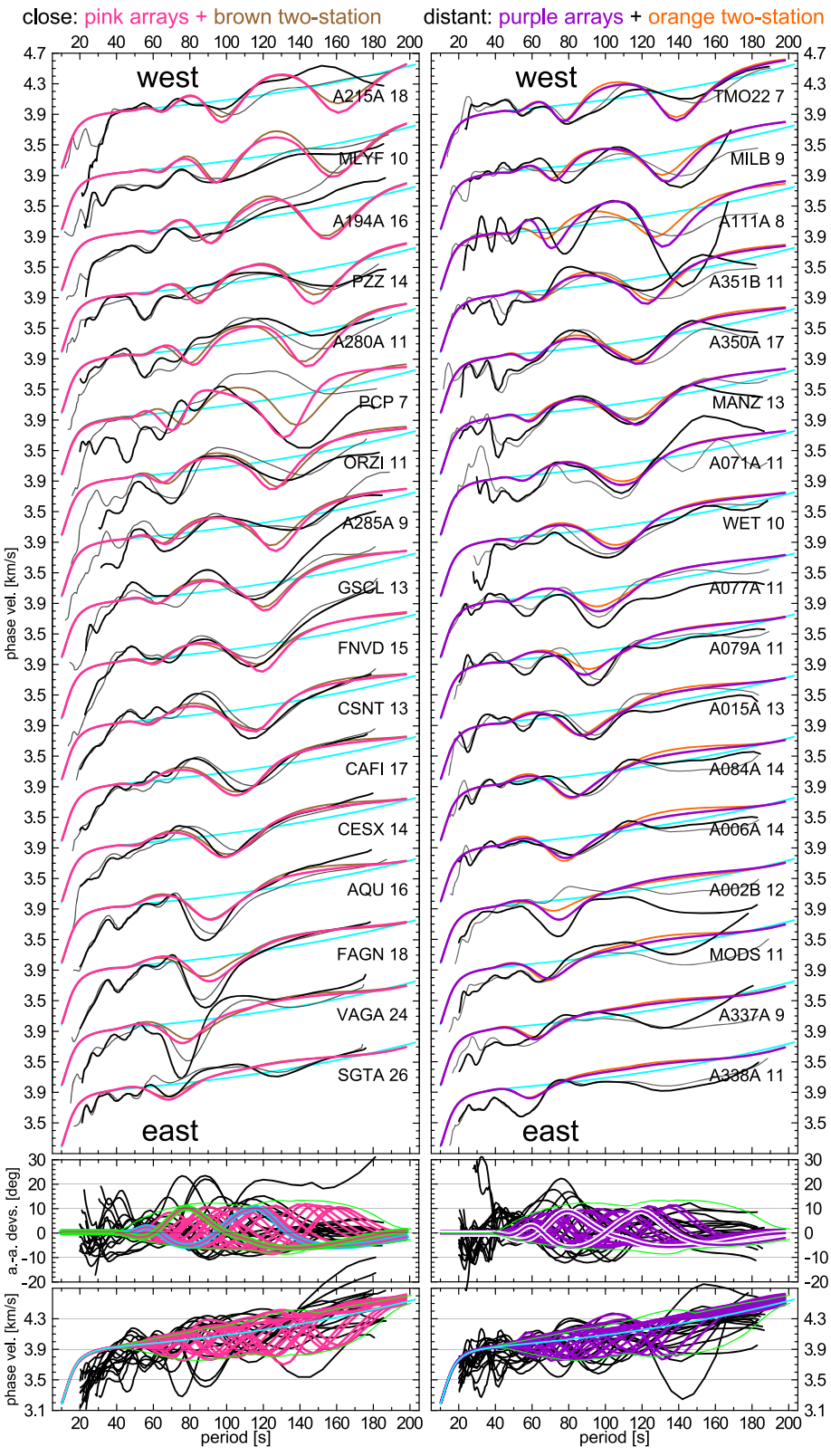

Figure 9. Dispersion curves measured on synthetic phase-time delays for two subarray sets (17 subarrays each). Pink curves correspond to southern subarrays (pink circles in Fig. 6), purple curves correspond to northern subarrays (purple circles in Fig. 6). Black lines are the dispersion curves measured using subarray on real data. Brown and orange are the synthetic dispersion curves from the two-station method for the two respective profile sets shown also in Fig. 6 (map) and Fig. 7 (dispersions). Grey are the respective two-station measurement using real data as in Fig. 7. These two two-station sets correspond in length to the size of the subarrays - see the brown profiles crossing the pink circles and orange profiles crossing the purple circles in Fig. 6. Bottom panels show the subarray dispersions and arrival-angle deviations merged for each set to show the range of values. Arrival-angle deviations emphasized by white, light blue and light green margins are used for examples, see text for details.

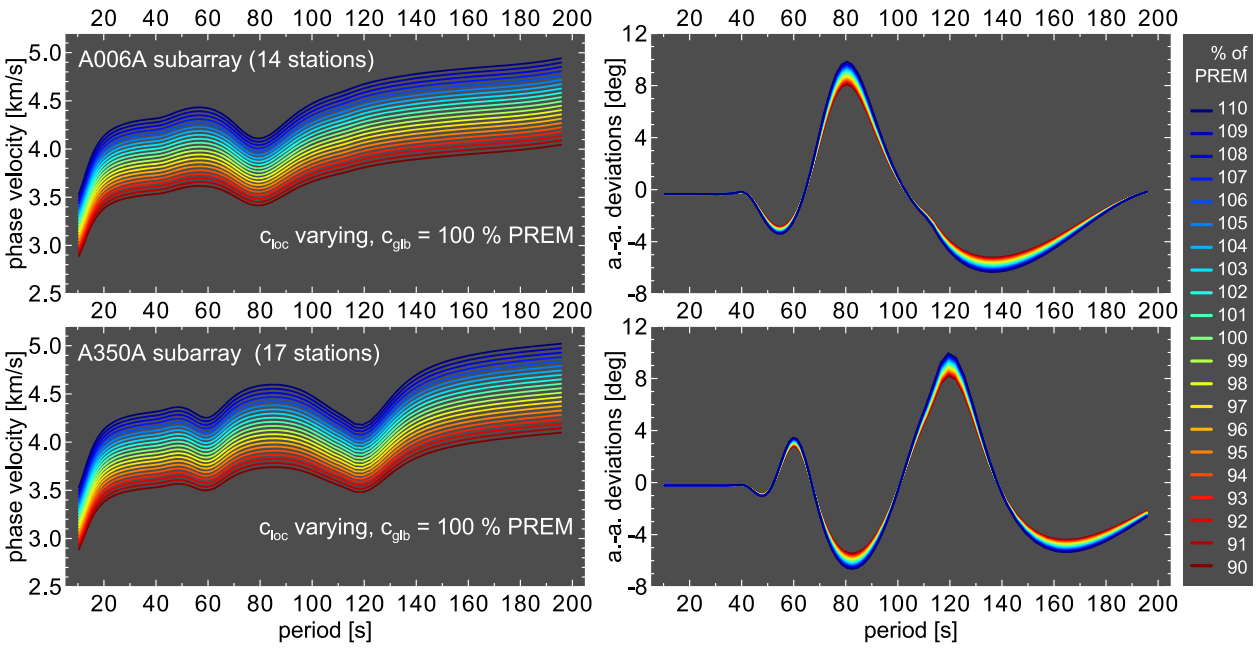

Figure 10. Set of 21 dispersion curves (left-hand panels) and arrival-angle deviations (right-hand panels) for two subarrays A006A (top panels) and A350A (bottom panels). Subarrays are shown by white circles in Figs 6 and 14, their respective arrival-angle deviations are also emphasized by white margins in Fig. 9. Phase velocity $c_{\rm loc}$ is varying and the phase velocity c_{glb} is kept constant (PREM). Colours denote the variation of $c_{\rm loc}$ with respect to PREM.

random. Velocities follow the trend of increasing values towards longer periods and arrival-angle deviations show the broadest scatter between 60 and 100 s with a 'neck' of very narrow range of values around 50–55 s. This arrival-angle deviation panel (c) corresponds to the colour maps inside the magenta-bordered AlpArray region in the first column in Fig. 4.

Next row in Fig. 8(e) and (f) represents the direct modelling of both arrival-angle deviations (e) and phase velocities (f) according to '(ii) *Direct modelling*' method described above. We calculated the arrival-angle deviations and phase velocities for each of the 499 subarray central stations using spatial differentiating of the phase-time delays when CVL model according to Fig. 2 is considered. Green lines in the panels (e) and (f) are taken as envelopes of all the values and are repeated also in the other three rows of panels (a–d) and (g, h) for comparison. The arrival-angle deviation panel in this row (e) corresponds to the colour maps inside the magenta-bordered AlpArray region in the second column in Fig. 4.

The last bottom pair of panels in Fig. 8(g) and (h) uses the same method of '(iii) *Measurement on synthetics*' as in the top pair (a, b), however, now for the phase-time delays modelled including the CVL anomaly as in the third pair of panels (e) and (f). Comparing directly the third and fourth pair of panels [(e) with (g) and (f) with (h)], we see that using the array measurement, we slightly underestimate the arrival-angle deviations which is due to the fact that arrays have larger aperture (±80 km) than what was used for the spatial differentiating (±10 km). Deviations are hence slightly smoothed. On the other hand, we slightly overestimate the range of dynamic phase velocities, see the small margins of black lines leaking out of the green envelopes in (h). The arrival-angle deviation panel in this row (g) corresponds to the colour maps inside the magenta-bordered AlpArray region in the third column in Fig. 4.

Results shown in Fig. 8 allows to draw an important conclusion. It is obvious that propagation of interfering waves causes the arrival-angle deviations [(c) and (g)]. But we obtain also wobbled dispersion curves [(d) and (h)] even the array beamforming already takes into account the arrival-angle deviations when calculating the velocity. In other words: knowing the 'true' arrival angle does not help to measure the structural velocity. It is still the dynamic phase velocity which we get. Looking only at the dispersion curves measured on real data (d), one could attribute all the differences among the 499 curves to the structure beneath the particular subarrays. However, the synthetic model (h) shows that most of the differences among the 499 curves are still due to the propagation effects having nothing to do with the local structure, which is the same for all the curves in (h). The green envelopes plotted over the curves measured on real data in (d) span a striking portion of the total velocity range of all the dispersion curves. This finding is close to the 'frustrating result' of Friederich (1998), who pointed out, that the data (phase velocities) can, in principle, be completely explained by the properties of the incoming wavefield not requiring any variations of the local structure at all.

To understand the wobbles emerging at the subarrays, we will look at a subset of subarrays in detail. Similarly as in the case of the two-station profile sets, we designed two sets of subarrays. Each set has 17 subarrays. Pink set is closer to the CVL anomaly and purple set is more distant. Both sets of subarrays are shown by respective colours in Fig. 6 by circles of 160 km in diameter. In addition, the pink subarray set was designed to correspond to the brown two-station set and the purple subarray set corresponds to the orange two-station set. It means that the shortest two-station profiles intersect the subarrays through their centres as far as the geometry allows and their lengths are as close to the 160 km of the subarray diameter as possible. This we use to compare the results of the two-station method and array beamforming at the same location. We do this comparison for both the real data as well as for synthetics. Results are shown in Fig. 9. Similarly as in Fig. 7, we plot the subarrays starting with the westernmost (most distant from the axis of symmetry) at the top continuing to the east at the bottom. Left-hand column is for (pink) subarrays closer to the anomaly

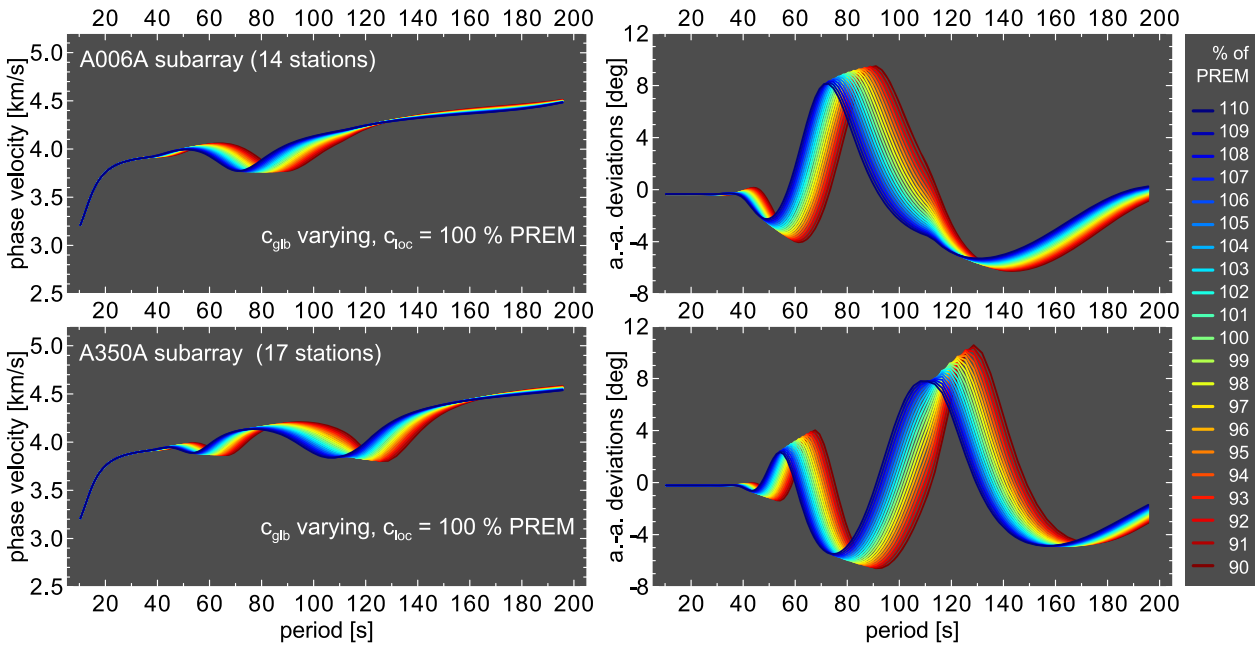

Figure 11. The same as in Fig. 10, but now c_{loc} is kept constant and c_{glb} is varying.

(epicentre), right-hand column shows subarrays (purple) in the north (more distant from the anomaly). Respective colour lines are used for the dispersion curves calculated using array beamforming on synthetic phase-time delays (pink and purple). Black lines are used to show the dispersion curves measured using the real data at each subarray. Behind the real and synthetic curves from subarrays, we redraw the dispersion curves from the first (brown) and second (orange) column from Fig. 7. Again, synthetics are shown by the respective colour (brown and orange), real data curves by grey lines exactly the same as in Fig. 7. The very first (westernmost) and the very last (easternmost) two-station profiles from Fig. 7 are not used because their position close to the edge of the network did not allow to construct subarrays at the same place. Each subarray is characterized by its central station name in Fig. 9, see also the map in Fig. 6. The number behind the central station name in Fig. 9 tells how many stations the particular subarray contains. At the bottom of Fig. 9, again similarly as in Fig. 7, we summarize all the 17 measurements together to see the ranges of values. The bottom panel shows phase velocities. Only subarray measurements are given in these summarizing panels (no two-station curves). In addition, we also present a summarizing panel for the arrival-angle deviations - this information cannot be obtained by the two-station method.

Comparing the synthetic and real data curves for subarrays (pink + black and purple + black), we again see general similarity. The match of data and synthetics is better for the middle (in the west-east direction) profiles. The main wobbles are pronounced in both the data and synthetics and the spatial shift of wobbles again follows the same trend both in data and synthetics, similarly as in the case of the two-station method shown in Fig. 7. One can easily follow the large negative wobble from around 145 s at the A280A subarray (pink) moving to 70 s at the easternmost SGTA subarray both in data and synthetics. The purple profile shows the negative long-period wobble shifting from 145 to 55 s across the whole set of 17 subarrays. Other positive/negative wobbles can be followed as well. Comparing the measurement on data for both methods (subarrays-black + two-station-grey lines) we see general similarity as well. The array-based dispersion curves themselves show the same features as those measured by the two-station method, see the points (i)–(viii) above. What is, however, the most striking is the similarity of the synthetic dispersion curves measured using subarrays and the two-station method (pink + brown and purple + orange) at their respective locations. There are differences but in general, the geometry of the subarrays and of the two-station profiles differs a bit as well.

There are, however, two lucky examples, where the geometry is almost ideal. The VAGA subarray (pink set, second from the bottom in Fig. 9) is intersected by the two-station profile IOCA-FRES with a length of 150.75 km, which crosses the central station VAGA and spans exactly the aperture of the subarray. In addition, this profile is perfectly aligned with the great-circle direction. This subarray is emphasized by a light green circle in Fig. 6. Looking at the synthetic dispersion curves at this spot in Fig. 9, we see that they are almost the same for the two-station method (brown) and for the subarray (pink). Moreover, the data dispersion curves are also very similar. In the summarizing arrival-angle deviation panel at the bottom of Fig. 9, the curve for the VAGA subarray is also emphasized by light green margins as is the circle in Fig. 6. The range of deviations spans from -6.1° (at period of 135 s) to $+10.3^\circ$ (at period of 78 s). In case of the two-station measurement, we do not know this deviation assuming simple propagation along the great circle. In case of the array measurement, we do know the angles and the velocity determination takes these into account. However, the velocity results of both methods are almost the same. Making and error of 10.3° in the propagation direction leaks in the velocity error of 1.6 per cent as $cos(10.3^\circ) = 0.984$. This is actually roughly the difference we see between the brown (IOCA-FRES profile) and pink (VAGA subarray) dispersion curves in Fig. 9 at their minima around 78 s. The velocities are 3.80 km s^{-1} for the two-station profile and 3.75 km s^{-1} for the subarray, the difference of 0.05 km s^{-1} represents 1.3 per cent. The remaining 0.3 per cent is attributed to the non-perfect geometry. Also note that the minimum is slightly shifted between the subarray (at 77 s) and the profile (at 79 s). The important thing to note is that the difference of both these dynamic

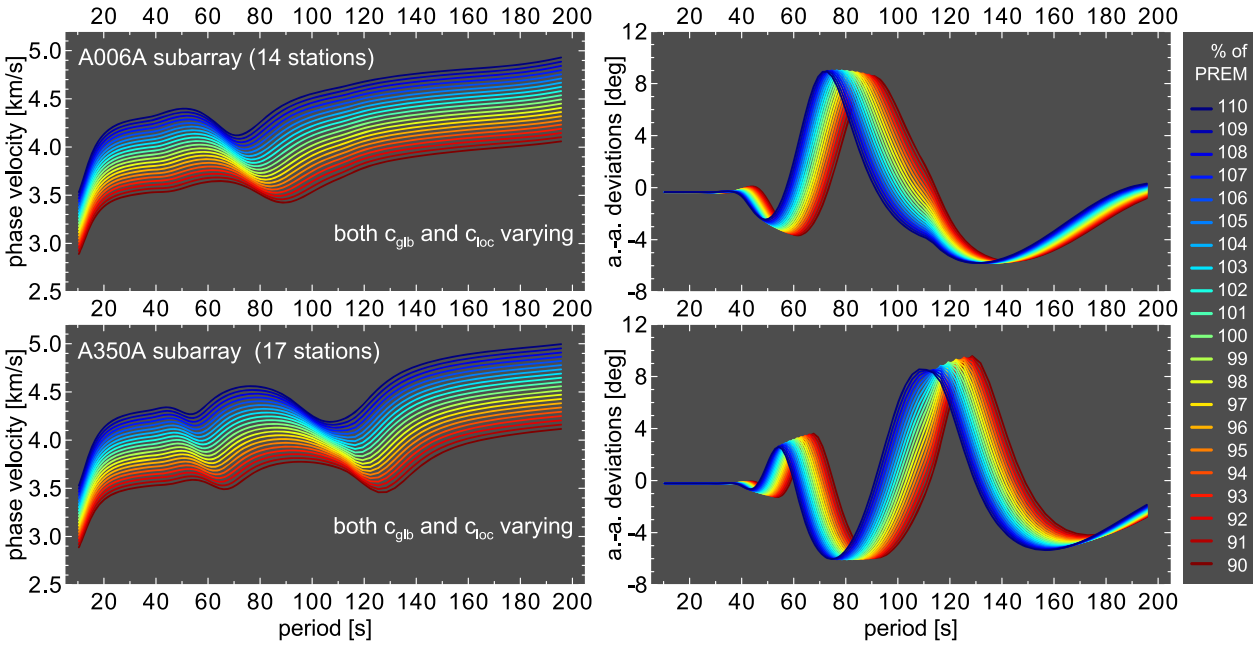

Figure 12. The same as in Figs 10 and 11, but both c_{loc} and c_{glb} are varying (simultaneously).

phase-velocity dispersion curves from the structural one (light blue curve for PREM) is 5.5 per cent (two-station method) and 6.7 per cent (subarray), as PREM has the velocity of 4.02 km s^{-1} at 78 s period. Similarly perfect geometry is found for the CSNT subarray (pink set, emphasized by light blue circle in Fig. 6) and CASP-LMD two-station profile (brown set, length of 158.31). We can draw similar conclusion for the CSNT subarray as well. Corresponding arrival-angle deviation curve for CSNT subarray is emphasized by light-blue margins in Fig. 9.

We see that knowing the arrival angle in case of subarrays does not make much difference when comparing the velocity to the two-station measurement. In addition, array measurement even does not make it necessarily better, as in the VAGA subarray case, where the two-station dynamic velocity is luckily closer to the PREM structural velocity than is the subarray dynamic velocity. Looking at the other example of the CSNT subarray (Fig. 9), we see that the two synthetic dispersion curves swap the positions when moving over the period range. At the minimum wobble around 120 s, the brown two-station curve is closer to the structural, at the maximum wobble around 80 s, it is the pink array curve, which is closer.

5.4 Modelling the wobbles

Up to now, we considered the phase velocity $c(T)$ of our medium being the same everywhere around the (CVL) anomaly. KB2019 used the same symbol 'c' in both the Eqs 2 and 4 therein (as well as KSB2020 used the same symbol in Eqs 1 and 3 therein). However, in general, we can consider these velocities to be different. This is the reason why we have labeled them by different subscripts in the rewritten Eqs (2) and (3) in the '4 Modelling' section of the current paper above. In Eq. (2), the phase velocity c_{glb} represents the velocity everywhere between the anomaly (scatterer) and the place of measurement (hence the subscript *global*). In Eq. (3), however, the c_{loc} represents the velocity right beneath the subarray (marked as *local* then). Let us see what happens, if we vary these velocities independently. As an example, we will measure the dispersion curves on synthetic phase-time delays for two subarrays at the purple set - A350A and A006A emphasized by white circles in Fig. 6, with respective arrival-angle deviations emphasized by white margins in the summarizing panels at the bottom of Fig. 9. These two subarrays have similar radial distance x to the anomaly (and epicentre), and they significantly differ by the lateral distance R to the axis of symmetry of the diffraction pattern. Fig. 10 shows what happens when the global c_{glb} is kept the same (as before at 100 per cent PREM) and c_{loc} is varying in the range of ± 10 per cent around PREM. There are 21 dispersion curves in the left-hand panels of Fig. 10 going from 90 to 110 per cent with a step of 1 per cent of the PREM velocity, plotted by different colours, see the legend in the right-hand side of the figure. The wobbles stay at the same position with respect to the period, as the c_{glb} is responsible for the shape of the whole diffraction pattern, which does not change. Not surprisingly, changing the local c_{loc} shifts the dispersion curves up and down. What is more worthwhile to note is the fact that for higher c_{loc} (blue lines), the wobbles are bigger. Arrival-angle deviations in the right-hand side panels (again 21 curves) also keep the same position of the maxima and minima. Higher local velocities produce higher deviations, what can be also directly seen from Eq. (3). The causal relation is as follows: because the arrival-angle deviations are higher for higher structural velocities (Eq. (3)), the deviation of the dynamic velocity from the structural (wobble) is bigger as well.

The second example shows the varying wobbles when the c_{loc} is kept constant and only the c_{glb} is varying. Fig. 11 follows the same layout as Fig. 10. We see that the dispersion curves stay roughly at the same velocities as c_{loc} is constant, and that the wobbles are shifting with period as the c_{glb} closes and opens the whole diffraction pattern. Decreasing the c_{glb} closes the pattern while increasing the period opens it, see Figs 12 and 13 in KB2019. If, at the same location, we would like to see the same wobble (a wobble corresponding to the same stripe of the interference pattern), with decreasing the c_{glb} (moving to red curves), we need to increase the period to compensate the lower c_{glb}. Arrival-angle panels show that the change of the amplitude of the deviations is much more pronounced than in the previous example. Decreasing the c_{glb} not

only changes the geometry of the pattern (closing it) but it also dramatically enlarges the arrival-angle deviations (red deviations span broader range of angles than blue deviations). This effect is larger for the subarray A350A which is more distant from the axis of symmetry.

The last example, given in Fig. 12, combines both the previous cases varying both c_{loc} and c_{glb} together. They move synchronously in this case. We see a combination of all previous changes: wobbles are changing their position with respect to period, they are changing its amplitude and curves are shifting up and down. Interesting to note is the difference between the two subarrays: as lower c_{loc} diminishes the arrival-angle deviations (Fig. 10) and as lower c_{glb} enlarges them (Fig. 11), varying both together yields nonintuitive results: At A006A the positive arrival-angle deviations decrease with decreasing both the velocities and at A350A the positive deviations increase. The negative ones do the opposite: they increase (in their absolute values) at A006A and decrease at A350A. We may also say that the deviations are shifting towards negative values for A006A and towards positive values for A350A when decreasing c_{glb} and c_{loc}. Everything anyway slightly trades-off with period.

Additionally, we may construct any combination of increasing/decreasing local and global velocities. The wobbles emerge as a complex combination of the subarray location and the diffraction pattern crossing that location. The diffraction pattern at given period depends on the distant heterogeneity properties (location, strength, geometry) and on the velocity along the path from the heterogeneity to the subarray. Moreover, the arrival-angle deviations are modified by the local phase velocity. Hence the wobbles can vary significantly for geographically close locations of subarrays. The main outcome of this exercise is to show how complex the behaviour is and that choosing the proper parameters, we can actually model the wobbles almost arbitrarily. This is to explain the discrepancy between the measurement of the real data and synthetics: in Figs 7 and 9, the modelling is simplified assuming the same phase velocity everywhere ($c_{loc} = c_{glb}$). Nevertheless, it still gives us the qualitative understanding of the phenomenon. Modelling with varying c_{loc} and c_{glb} (not even mentioning that c_{glb} does not need to be homogeneous over the whole wavefield path as well as c_{loc} does not need to follow variations of the PREM but it can be much more complex) would give us better match between the data and synthetics. The point of our paper is, however, not to fit the data with the model, but to show the principles governing the phase-velocity wobbles emergence.

5.5 How non-plane are the non-plane waves?

We will now investigate, what happens with the shape of the wavefront, when surface waves are affected by the interference after the CVL anomaly diffraction. As an example, we will use again the two subarrays as in the previous figures, namely A350A and A006A, see white circles in Fig. 6. Fig. 13 shows four panels for A350A subarray (left-hand panels) and the same panels for A006A subarray (right-hand panels). At the top, we plot the arrival-angle deviations. Purple lines show the synthetic (as both subarrays belong to the purple set, see Figs 6 and 9) and black lines the measured deviations using the real data. These synthetic curves are the same as those emphasized by white margins in the summarizing panel at the bottom of Fig. 9 (right-hand side). We see qualitatively good match between the synthetics and data. The second row of panels of Fig. 13 shows the dispersion curves. Again, purple lines are for synthetic and black for real-data curves. These curves are the same as in Fig. 9 (right-hand panel). We also see qualitatively matching velocity wobbles between synthetic and real-data dispersion curves.

As explained in KB2019, when fitting the plane into the measured time differences of the subarray (linear regression), we obtain time residuals, which tell us, how much the actual measurement deviates from the fitted plane. These residuals were used to assess the data quality in the KB2019 paper. In case of synthetics, however, the 'data' quality is perfect. In this case, the residuals can be used to quantify the curvature of the wavefront from the plane. The third row of panels in Fig. 13 shows the residuals for each of the neighboring stations (16 in case of the A350A subarray and 13 in case of the A006A subarray). We see the residuals wiggling in the range of ± 1.4 s creating a pattern, where high positive residual at some station is followed by negative residual of almost the same shape (mirrored) at different station. To obtain a common measure of the curvature of the wavefront across the whole subarray, we calculate a mean residual, which is an average of the absolute values of all these individual residuals for each period. These mean absolute residuals are plotted in the bottom panels of Fig. 13 by dark blue lines. In addition, the black lines in the bottom panels show the residuals for real data. The shape is similar, especially for the A006A subarray. These real-data residuals are, of course, higher, containing also the measurement and real-data errors and noise.

Black vertical lines mark the positions of local minima of the mean absolute residuals with respect to the period range. Solid black lines are used for residual minima, which correspond to high phase-velocity deviations in the second row of panels. Dashed black lines are used for residual minima corresponding to the velocity lows. We see that whenever the mean absolute residual is low, the dynamic phase velocity has locally the highest deviation from the structural phase velocity (showed by cyan line for the PREM in the second row of panels). Also, at these periods, where the velocity is deviated the most, the arrival-angle deviations are (locally) the highest. Qualitatively, the mean absolute residual behaves as a derivative of the velocity (and arrival-angle deviations) with respect to the period. It means that the wavefront is the closest to the plane wave at the periods where the discrepancy between the structural and dynamic velocity is the highest. It goes against the common belief that plane wave gives us the 'true' velocity. It is rather the opposite. Hence, assuring the planarity of the wavefronts does not help to determine the structural velocity.

Fig. 14 shows two maps for two periods (80.4 and 67.7 s) marked by vertical green lines over all panels in Fig. 13. Synthetic arrival-angle distribution is shown by the colour background in Fig. 14. The colour scale is the same as in Figs 2–4. At 80.4 s, subarray A350A is situated in the maximum of a negative arrival-angle deviation stripe while subarray A006A is situated in the maximum of a positive stripe. Both subarrays (shown in Fig. 14 by white circles, the same as white circles in Fig. 6) show a minimum of mean absolute residuals in Fig. 13 for the period of 80.4 s, meaning the wavefront is almost a plane wave. This wavefront is plotted in Fig. 14, top map, by dark blue lines, which correspond to every 2 s of propagation of the 80.4 s Rayleigh wave with the velocity of 4.030 km s^{-1} (PREM) after passing the CVL anomaly of the width of 374.3 km and $\tau_{max} = 46.38$ s, as set by the CVL model in Fig. 2. For comparison, we plot also the circular PREM wavefronts by cyan lines. The mean absolute residuals for these PREM wavefronts are shown in the bottom panel of Fig. 13 as well by cyan line. Note that these are not zero, but have the value of 0.02 s across the period range. This is because the modelled PREM wavefront is circular, not

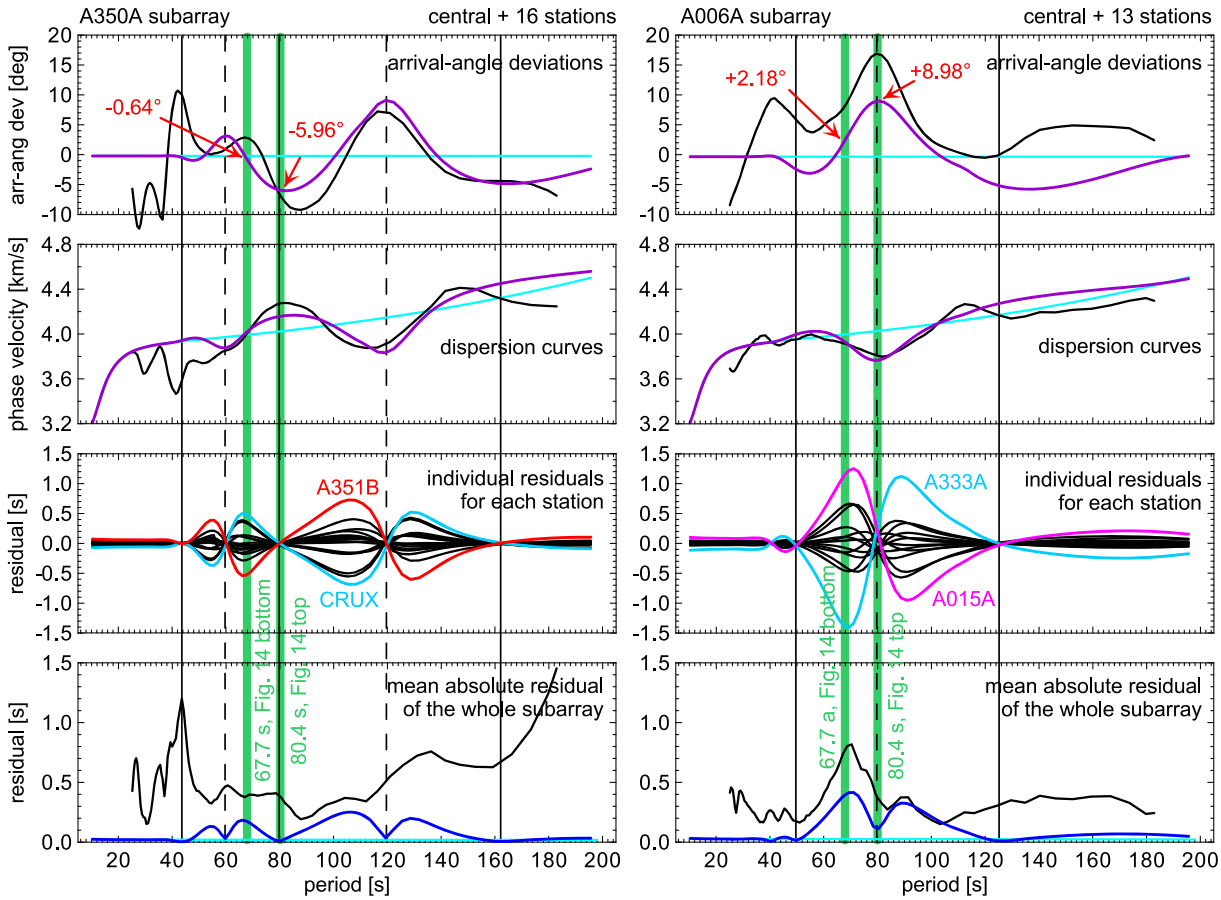

Figure 13. Arrival-angle deviations, dispersion curves and time residuals for two subarrays are shown for real data, synthetic model with CVL anomaly and synthetic PREM (1-D model only). Black vertical lines denote the residual minima, solid black corresponding to high-velocity deviation and dashed black for low-velocity deviations. Green vertical lines show the two periods (67.7 and 80.4 s) discussed in Fig. 14 (see text).

planar. The radius of that circle (wavefront curvature) is the same for all periods. In Fig. 14, we see how the CVL-anomaly wavefronts deviate from the PREM circular wavefronts. To emphasize the difference, cyan arrows show the propagation along the great circle and dark blue arrows show the propagation direction obtained from the subarray measurement by fitting a plane into the distorted CVL-anomaly wavefronts. The respective arrival-angle deviations are labeled in both Figs 13 and 14 as well (-5.96° for A350A and $+8.98^\circ$ for A006A). These high arrival-angle deviations correspond to high difference between the structural and dynamic phase velocity (Fig. 13): the wobble is positive in the case of the A350A subarray (green vertical line at 80.4 s coincides with the solid black vertical line in Fig. 13) and negative in the case of the A006A subarray (green vertical line at 80.4 s coincides with the dashed black vertical line in Fig. 13). Dashed white lines in Fig. 14 show the great circles from the epicentre, the same as in Fig. 6. The dark blue CVL-anomaly wavefronts inside the white-bordered subarrays are highly deviated from the great-circle wavefronts, however, they are still almost perfectly plane for the period of 80.4 s. The opposite is seen in the bottom map of Fig. 14, where the same is plotted for the period of 67.7 s. Both subarrays are now situated in the regions of very low arrival-angle deviations (white colour of the background) and also the dynamic and structural velocities are almost the same (Fig. 13). The period of 67.7 s is also emphasized in Fig. 13 by vertical green line plotted over all the panels. Again, in Fig. 14, bottom panel, we show a CVL-anomaly-distorted wavefront for every 2 s of propagation at 67.7 s period of Rayleigh wave with the velocity of 3.998 km s^{-1} (PREM) passing the CVL anomaly of the width of 387.0 km and $\tau_{max} = 32.96$ s (see Fig. 2). The arrival-angle deviations at both subarrays are small (again labeled in both Figs 13 and 14, having the values of -0.64° and $+2.18^\circ$ for A350A and A006A subarray respectively), however, the residuals are now much higher at the period of 67.7 s than they were in the previous case at period of 80.4 s showing that the wavefront is actually very curved. While before, at the period of 80.4, we had almost perfectly plane wave and the discrepancy between the dynamic and structural velocity was high, now, at 67.7 s, where the dynamic velocity is almost equal to the structural, the wavefront is actually very curved. We see that high arrival-angle deviation means high discrepancy between dynamic and structural velocity even the wave is almost planar. Low arrival-angle deviation means that dynamic velocity is almost equal to the structural and the wavefront is significantly curved.

In both Figs 13 and 14, we marked also the stations with the highest individual residuals. These are A351B (red line in Fig. 13 and red triangles in Fig. 14) and CRUX (light blue line in Fig. 13 and light blue triangles in Fig. 14) stations for the A350A subarray. The same for A015A (magenta line in Fig. 13 and magenta triangles in Fig. 14) and A333A (light blue line in Fig. 13 and light blue triangles in Fig. 14) stations for the A006A subarray. Not surprisingly, the

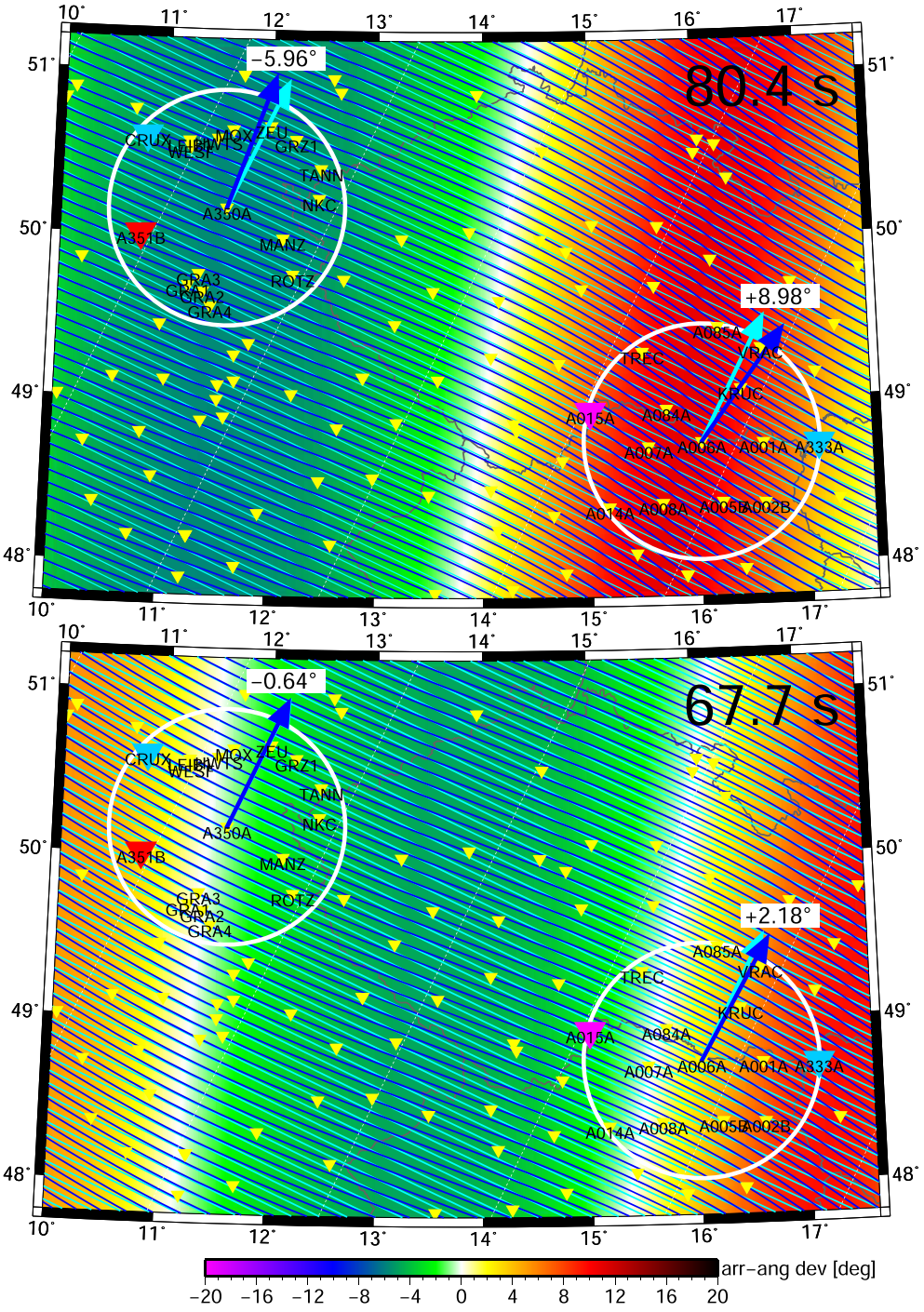

Figure 14. Arrival-angle deviations (colour map, the colour scale is the same as in Figs 2–4), PREM circular wavefronts (cyan) and CVL anomaly synthetic wavefronts (dark blue) shown in detail for two subarrays from Fig. 13 (dispersions shown in Figs 10–12, location shown in Fig. 6 by white margins behind the purple circles). Dashed white lines show the great circles from the epicentre, cyan and dark blue arrows denote the propagation direction of the PREM and CVL-anomaly wavefronts, respectively.

stations with the highest residuals are always at the outer edges of the subarrays.

6 DISCUSSION

Looking at the papers mentioned in the introduction, and also in the Appendix, section ‘A.5 Possible explanation’, we see that there has always been a general agreement on the wobbles being caused by interference of the fundamental mode of surface waves with different wavegroups. The studies differ by suggesting, what are these interfering waves: Brune & Dorman (1963) - Sa and Sn waves, Pilant & Knopoff (1964) - multiple events, Knopoff *et al.* (1966) - multipathed wave trains, Knopoff & Mal (1967) - back reflection from inclined Moho, Thatcher & Brune (1969) - mode interference, Dziewonski (1970) - lateral refraction, Capon (1970) - refraction at continental margins, Weidner (1972, 1974) - interference caused by

waves scattered from the Mid Atlantic Ridge. Our paper connects with the idea of Weidner (1972, 1974) confirming the wobbles being caused by the interference of a single mode of the same surface-wave type (fundamental mode of Rayleigh waves). We do not deny the other explanations. They take place in certain cases. However, we say that the main portion of wobbles seen at the dispersion curves measured using the records on AlpArray seismic network from the earthquake propagating from the South Atlantic Ocean are caused by interference of diffracted fundamental-mode Rayleigh waves after passing the CVL anomaly in Central Africa. We have collected evidence which effectively excludes other explanations. These are namely the points (i)–(viii) in the section '5.2 Results - Two-station method'. Let us give some comments to these points.

(i)–(iii): Points (i)–(iii) talk about the geometry of the interference (diffraction) stripes of arrival-angle deviations (phase-time delay) which cause characteristic amplitude of the wobbles being bigger when the measurement is closer to the anomaly, more distant from the axis of symmetry and when the profiles are shorter. Especially the fact that shorter profiles have bigger wobbles is interesting. For the two-station method, a limiting condition is usually used. Profiles need to be longer than a certain distance (Legendre *et al.* 2014 - 250 km; Mitra *et al.* 2006 - 200 km; Prindle & Tanimoto 2006 - 150 km; Foster *et al.* 2014 - 100 km). Sometimes, the authors note that if the distance is too short, the measurement does not work (Meier *et al.* 2004, Baumont *et al.* 2002; Bourova *et al.* 2005). However, no explicit reason is usually mentioned for that, besides general statements that the measurement is more stable for longer paths and that shorter profiles are more affected by noise. Of course, measurement errors play a role. For closer stations, the relative error is higher as the measured time difference is smaller (Bourova *et al.* 2005; Foster *et al.* 2014). Our synthetic phase-time delays, on which we measure the interstation phase velocity, however, have no measurement errors and we still see the wobbles for both short and long profiles. We now have a clear explanation as to why the shorter profiles suffer by higher wobbles. They are more likely to span right from one negative to the other positive stripe of phase-time delays causing the highest apparent velocity difference between the stations. There is no clear limiting distance of the two stations, below which the two-station method does not work and above which it does. The longer the two-station profile is, the smaller are the wobbles, but the wobbles are still present for any distance. The green envelopes of arrival-angle deviations and phase velocities from Fig. 8(e) and (f) are not only copied to the other panels of the same figure, but for comparison, we also repeat them in Fig. 7 (two-station method) and Fig. 9 (subarrays). While in Fig. 9, the pink and purple sets of subarrays obviously fit into the envelopes, as the envelopes are calculated using all the 499 subarrays and Fig. 9 shows a subset of these 499 subarrays, the comparison in Fig. 7 is more interesting. It clearly shows that while the brown two-station set (the closest to the anomaly and of the shortest lengths) spans the whole range of subarray velocities, all the other four two-station profile sets span smaller range of velocities, as they are either longer or more distant from the anomaly than the brown two-station set. We can say that subarrays velocity estimation performs as badly as the shortest two-station profile estimation. Note that we are still talking about 'bad' performance in terms of the discrepancy between the structural and dynamic velocity. The array measurement itself performs well. As shown also by Pedersen *et al.* (2003) and Bodin & Maupin (2008), arrays can be used to measure phase velocities of wavelengths ten times longer than is the array aperture. In other words, the measurement is correct, just the velocity we obtain is always only the dynamic one.

In case of the two-station method, sometimes, instead of a fixed limiting (smallest) distance between the two stations, a relation to the wavelength is used (Meier *et al.* 2004 - a general comment on that one of the profiles is too short with respect to wavelength; de Vos *et al.* 2013 and Ekström 2014 - interstation distances longer than two wavelengths are used; Wu *et al.* 2020 - using only wavelengths shorter than the station distance). In our modelling, for a given profile length, the wobbles may seem to be bigger for longer waves (at 140 s, they are bigger then at 80 s). The reason is, however, not the interstation distance, but the size of the CVL anomaly, which appears stronger for longer waves. As the CVL almost disappears for waves over 180 s in our modelling, the wobbles disappear as well even for the shortest profiles. Of course, real data suffer by the measurement errors. However, we again do not see any limiting interstation distance compared to the wavelength in case of the two-station method.

(iv): Point (iv) in Section 5.2 says that the match between synthetic and real curves is the better, the longer the profiles are. This is caused by two independent reasons: Longer profiles give us more averaged structural information, which tends to be closer to the PREM used for calculating the synthetics. In the same time, the wobbles are getting smaller as the longer profiles span bigger portion of diffraction stripes averaging also the effect of different phase-time delays.

Another interesting observation is that the wobbles are bigger for profiles (both from the two-station method as well as from subarrays) that are more distant from the axis of symmetry (even when the radial distance to the anomaly and source is kept the same). This is obvious from all the seven sets of profiles in Figs 7 and 9, where the wobbles at the top (west, more distant) are always bigger than the wobbles at the bottom (east, closer to the axis of symmetry). This observation is connected with the fact that the outer lobes of arrival-angle deviations have larger amplitude than the central lobes. This 'swap' of amplitudes happens after a certain distance from the anomaly, and it happens the closer to the anomaly, the longer the waves are. That can be seen in Fig. 4 at the background arrival-angle deviation maps. For the period of 49.2 s, the first positive lobe clearly dominates the pattern at the radial distances (from the anomaly and from the epicentre) of AlpArray region. However, at the period of 66.2 s, the first and second positive lobes has equal amplitudes and for periods longer than 89.0 s, the second positive lobe has clearly higher amplitude than the first one. When we move to the longest periods, we see the same for the arrival-angle deviations gradually becoming higher at the third lobe than are those at the second lobe. When we look at a single period, for example 89.0 s in Fig. 4, the first positive lobe has clearly decaying amplitude with the radial distance (it is more red in the south and only yellow in the north), the second positive lobe keeps its amplitude roughly constant over the span of the map and the third positive lobe clearly increases its amplitude with the radial distance (it is more red in the north and yellow in the south). The same is also seen in Fig. 2 for the 100 s wave. Figs 3, 6, A1 and B1 in KSB2020 show the same.

The latter paper also suggests an explanation for this observation, see KSB2020, Appendix D - The Yellowstone plume. The phase-time delays of outer lobes have smaller amplitudes than those of the first lobe. However, the lobes are getting narrower with the lateral distance from the axis of the symmetry. As the arrival angles (and hence also the phase-velocity wobbles) are given by the spatial derivative of these phase-time delays in the lateral direction, and as these phase-time delays are varying over shorter distances, the derivatives are getting higher. Following Liu & Holt (2015), the Appendix D in KSB2020 deals with the gradiometry coefficient $\vec{B}$,

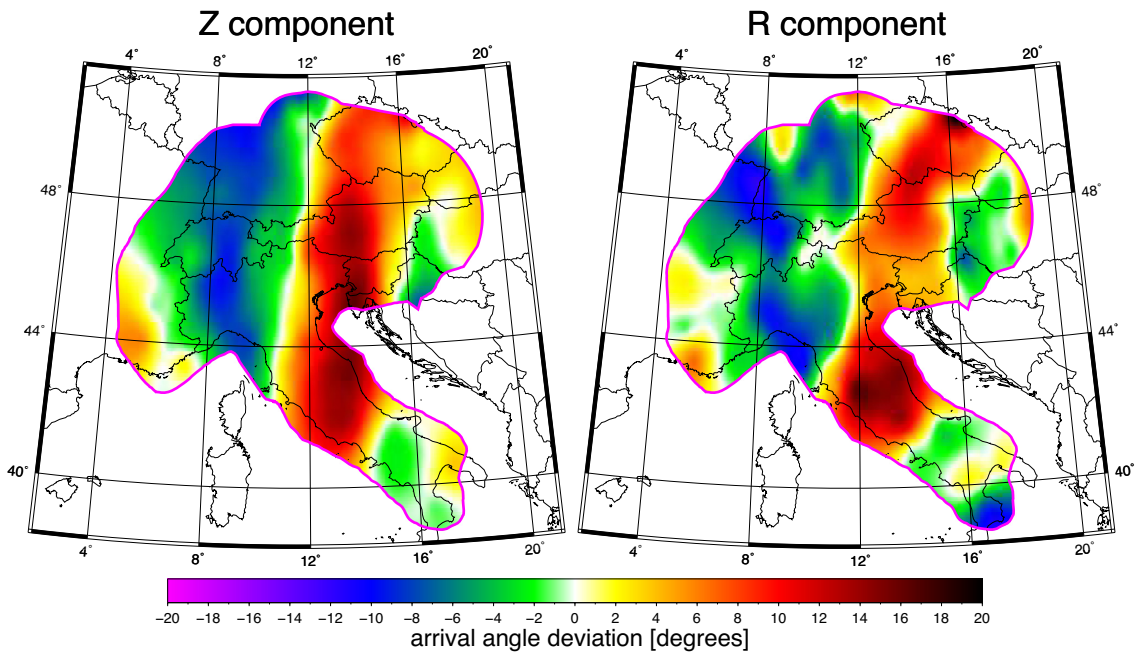

Figure 15. Arrival-angle deviations for 100 s Rayleigh wave measured from the $M = 7.4$ earthquake in the South Atlantic Ocean on vertical Z and radial R components. Left-hand plot corresponds to Fig. 4 of the current study and also to Fig. 3 in the KSB2020 paper.

(negative slowness). Fig. D1 in KSB2020 shows the pattern of $\nabla.\vec{B}$ (the divergence of $\vec{B}$), which is a second spatial derivative of the phase-time delays. Arrival-angle deviations are only a first spatial derivative of the same delay times. The second derivative enhances obviously even more the outer lobes. This is why we see so many outer lobes of $\nabla.\vec{B}$ in Fig. D1 in KSB2020.

(v): Shifting pattern of wobbles. This spatial match between the wobble pattern, which is preserved both in the data as well as in synthetics for both the two-station profiles as well as for subarray measurements, could be hardly achieved by any other explanation. AlpArray network allowed to perform a two-station measurement at 95 profiles with ideal geometry sampling the region with unprecedented density of paths. The fact that we see a consistent shift of the wobbles with period when moving the profiles from west to east supports the proposed mechanism of wobble emergence the best.

(vi): Wobbles are more stretched along the period range for longer waves. This can be generalized to point out that the wobbles are repeating across the period range. In other words: the stretch of the wobbles towards longer periods is observed because the wobbles are repeatedly taking place over the whole period range. If there was only one wobble, we could not talk about stretching of the others. Explanations like the steps in Moho yield only limited number of wobbles (three) at certain period range which is sensitive to the given depths (Knopoff & Mal 1967). Observing the wobbles over broad period range again supports the idea that their cause must be spanning broad range of depths.

(vii): The shorter the profiles are the more complicated are the real-data dispersion curves at shorter periods. There are two reasons for that. One can be attributed to the structure (inverse to what is stated in point (iv)): Longer profiles are averaging the structural heterogeneity while the shorter ones are reflecting the complexity of the locality. Second reason follows the dynamic behaviour of the wobble emergence: Shorter profiles have always bigger wobbles as discussed under (i). Even it is not modelled below 40 s in our case, the interference still takes place there as well. The diffraction is not necessarily caused by the CVL - it can be due to any other anomaly, maybe closer to the network, smaller in scale affecting rather the shorter wavelengths. The wobbles at the real-data dispersion curves for short period anyway follow the rule (vi) that they are wiggling faster along the period axis. However, this fact does not help to distinguish between the structural and dynamic effects, because also the sensitivities of surface waves to the structure are narrower in the period range for particular depths (Brune & Dorman 1963; Novotný 1970; Novotný *et al.* 2005).

(viii): The real data have, in general, bigger wobbles than the synthetics. This is an issue mentioned already by KSB2020. While inverting for the diffraction pattern across the AlpArray, the modelled arrival-angle deviations were systematically lower than the observed ones. We could not simply make the CVL anomaly stronger. It would lead to higher deviations, but it would, at the same time, change the geometry of the pattern significantly. The model of CVL anomaly given by KSB2020 is based rather on fitting the geometrical pattern of the stripes even though the amplitude of the deviations were not matched completely. A proposal how to explain this issue is given by the modelling presented in Figs 10–12 of our current work. The arrival-angle deviations are affected both by the global phase velocity c_{glob}, which shapes the geometry of the pattern and gives rise to the main portion of the deviations, as well as by the local phase velocity c_{loc} under the subarray (two-station profile), which may still increase the deviations significantly (without changing their position in the period range). Including the real velocities both for the global wavefield propagation as well as for the local subarrays would lead to a better fit between the real data and synthetics. However, neither KSB2020 nor our current work aimed to explain every detail. The goal was and still is to explain the principles.

We used Rayleigh waves measured on the vertical component. An obvious question is, whether the Rayleigh waves measured on the radial component behave the same. As a quick answer, we processed the records on the horizontal component showing the results in Fig. 15. Left-hand plot is the map of arrival-angle deviations at

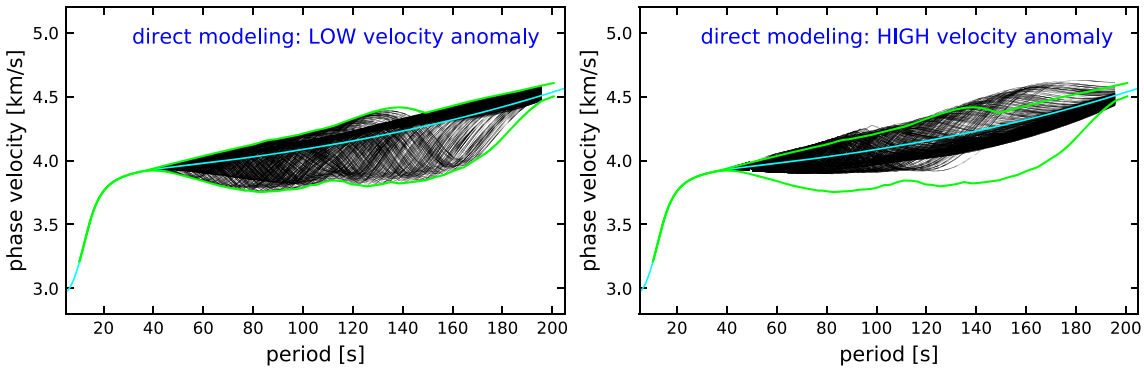

Figure 16. Left-hand panel is a copy of panel (f) from Fig. 8 showing 499 phase-velocity dispersion curves calculated for the low-velocity anomaly under the CVL. Right-hand panel shows dispersion curves calculated for the high-velocity anomaly of the same size and location. Green envelopes and light blue PREM curves are the same in both panels.

100 s period wave for the vertical component, the same as in Fig. 3 of the KSB2020 paper and similarly as in Fig. 4 of this paper (where only the measurement at different periods are shown). The records for the radial component were processed using exactly the same parameters (filter widths, tapering length) as for the vertical component. As the signal-to-noise ratio is generally worse for the horizontal component, we needed to remove 13 stations (2.6 per cent out of 499) with respect to what has been used for the vertical, at which we could not clearly identify the fundamental mode. Even the subarray measurement suffers by higher residuals in case of the horizontal component, the similarity of the two maps in Fig. 15 is obvious.

Our modelling shows that the difference between the dynamic and structural velocity can easily reach −9.9 per cent (at 150 s) or +4.8 per cent (at 130 s), see the envelopes in Fig. 8 differing from the PREM. For the real data, this difference is probably even larger. We cannot quantify it exactly not knowing the real structural velocity. In any case, this discrepancy is much larger than any error made by not knowing the arrival angle in case of the two-station method, where we end up with a difference of 1–2 per cent. The reason, why the two-station method sometimes gives us a velocity even closer to the structural one than the array is that sometimes the two-station profile can luckily coincide with the deviated arrival angle measuring hence purely the dynamic velocity not affected by any angular deviation. During the linear regression when using the array, the arrival direction is always necessarily compromised by fitting a plane into many measurements.

The heterogeneity found under the CVL in KSB2020 is a low-velocity anomaly. The modelling in our current paper follows the results of KSB2020 using the low-velocity anomaly as a source of the diffraction. Fig. 8(f) and (h) presents the dispersion curves directly modelled and measured by subarrays on synthetic time delays. The dynamic velocities, in general, have the wobbles more pronounced towards lower velocities. The cloud of 499 black wobbled dispersion curves deviates two times more down from the structural PREM curve (light blue) by up to −9.9 per cent in contrast to the deviations towards higher velocities (up to +4.8 per cent, see also the paragraph above). The question is, how this asymmetry is related to the sign of the anomaly. Fig. 16 gives the answer. On the left-hand panel, we show exactly the same curves as in Fig. 8, panel (f). These are 499 phase-velocity dispersion curves directly modelled using the low-velocity CVL anomaly results from KSB2020. The right-hand panel in Fig. 16 shows again 499 curves, modelled for a hypothetical anomaly with the opposite sign, meaning for a high-velocity anomaly. All other parameters (width, strength, location, background velocities) are kept the same. Green envelopes and the light blue PREM curve from the left-hand panel are copied to the right-hand panel for comparison. We see that the asymmetric behaviour of the diffraction pattern produced by the high-velocity anomaly with respect to the low-velocity anomaly, as discussed in KSB2020 and shown in the Appendix C therein, is transformed to asymmetric behaviour of the wobbles. While the high-velocity anomaly wobbles which deviate to higher velocities are almost the same as in the case of the wobbles from the low-velocity anomaly, the wobbles towards low velocities do not deviate that much in case of the high-velocity anomaly. In case of the high-velocity anomaly, the wobbles are bit more symmetrically distributed around the structural PREM curve. This may also explain, why in Fig. 8(d), we again see that the dispersion curves measured on real data deviate from the PREM model much more towards lower values than towards higher values. However, remember that the measurement on real data still reflects the heterogeneous structure under the Alps, which the synthetics do not.

The principal difference between the structural and dynamic phase velocity was given by Wielandt (1993). As our work perfectly fits to his explanation of phase velocity being affected by interference of different waves, we keep the terms ‘structural’ and ‘dynamic’ throughout our paper as well. Wielandt (1993) suggested that the dynamic (measured) velocity could be recalculated to the structural (desired) one by using the second spatial derivatives of the amplitudes of the wavefield. Later, this approach was confirmed by modelling in Bodin & Maupin (2008) and used by, for example Liu & Holt (2015). Interestingly, the use of the amplitude information works without knowing the specific cause of the interference. Showing the possibility to reveal the actual cause of the interference by modelling the wavefield propagating after a particular scatterer in our current study opens the question, whether knowing the cause could be used to recalculate the dynamic velocity to the structural one using other means then the amplitude distribution, which is difficult to measure. The simplest approach would be obvious: being able to model the wobbled dispersion curves, one can subtract the wobbles from the measured curves attributing then the ‘cleaned’ velocity to the structural velocity. This, however, would need more sophisticated modelling approach, as the wave propagation needs to be modelled in 3-D all the way from the anomaly to the stations.

7 CONCLUSION

We have shown, how the fundamental mode Rayleigh waves propagating from the South Atlantic Ocean and passing the Cameroon Volcanic Line anomaly in the upper mantle beneath Central Africa give rise to phase-velocity dispersion curves suffering by wobbles when measured across the AlpArray network in Europe by two different methods. The main point of our work is to introduce the principle how the wobbles emerge due to the interference of diffracted wavefield. The specific earthquake location and the particular anomaly causing the scattering of the waves is used here to demonstrate the approach. Showing the results of the two-station method as well as array measurement, we conclude that in principle, they are both affected by the interference in the same way. Even knowing the arrival angle is a valuable information, arrays do not perform better than the two-station method when it comes to estimating the structural velocity. The difference between the structural and dynamic velocity can be several times higher than the error made by unknown arrival angle. We have also proposed a method to model the dynamic dispersion curves of an interfering wavefield propagating in 1-D structure. The similarity of the spatial pattern of the wobbles as well as their position across the period range allow to conclude that the main portion of the observed phase-velocity deviations, which cannot be explained by the structure, is due to the interference of the direct and scattered fundamental mode.

ACKNOWLEDGEMENTS

We acknowledge financial support by the Austrian Science Fund (FWF) through project P 26391–AlpArray Austria and P 30707–AlpArray Austria 2. The Python Toolbox ObsPy by Beyreuther *et al.* (2010) was used for data pre-processing. Maps were plotted using Generic Mapping Tools by Wessel *et al.* (2013). Comments and suggestions by Wolfgang Friederich and Éric Beucler helped to improve the paper and are highly appreciated.

We acknowledge the operation of the AlpArray temporary seismic network Z3, see Hetényi *et al.* (2018) and AlpArray Seismic Network (2015) and the permanent seismic networks used in this study: BA (Universita della Basilicata Seismic Network), BW (Department of Earth and Environmental Sciences Geophysical Observatory University of Munchen 2001), CR - University of Zagreb (2001), CZ (Czech Regional Seismic Network Institute of Geophysics Academy of Sciences of the Czech Republic 1973), FR (Reseau sismologique et géodésique français 1995), G (Institut de physique du Globe de Paris and Ecole et observatoire des sciences de la terre de Strasbourg 1982), GE (GEOFON Data Centre 1993), GR (German Regional Seismic Network Federal Institute for Geosciences and Natural Resources (BGR) 1976), GU (University of Genova 1967), HU (Kövesligethy Radó Seismological Observatory Geodetic And Geophysical Institute Research Centre For Astronomy And Earth Sciences Hungarian Academy Of Sciences 1992), CH (Swiss Seismological Service ETH Zurich 1983), IV (Istituto Nazionale di Geofisica e Vulcanologia 2006), IX (Irpinia Seismic Network, Unit of experimental and computational seismology, Physics Department, University of Naples Federico II, Italy), LC (Laboratorio Subterraneo de Canfranc Spain 2011), MN (MedNet Project Partner Institutions 1990), MT (National French Landslide Observatory Facility and Reseau sismologique et géodésique français datacentre 2006), OE (Austrian Seismic network Zentralanstalt für Meteorologie und Geodynamik 1987), OT (University of Bari 'Aldo Moro' 2013), OX (Istituto Nazionale di Oceanografia e di Geofisica Sperimentale 2016), PL (Polish seismological network, Institute of Geophysics, Polish Academy of Sciences), RD (Réseau Sismologique et géodésique Français 2018), SI (Province Südtirol, Zentralanstalt für Meteorologie und Geodynamik, Austria), SK (Earth Science Institute Slovak academy of sciences 2004), SL (Slovenian Environment Agency 2001), ST (Geological Survey Provincia Autonoma di Trento 1981), SX (Leipzig University 2001), TH (Thüringer Seismologisches Netz Friedrich-Schiller-Universität Jena 2009). The data from the permanent networks can be freely accessed by the ORFEUS/EIDA repository. The data from the AlpArray temporary seismic stations (Z3) can be accessed the same way after being open to the AlpArray Working Group (1. April 2020) and to the general public (1. April 2022).

The authors would like to thank to the AlpArray Seismic Network Team: György Hetényi, Rafael Abreu, Ivo Allegretti, Maria-Theresia Apoloner, Coralie Aubert, Simon Besançon, Maxime Bès De Berc, Götz Bokelmann, Didier Brunel, Marco Capello, Martina Čarman, Adriano Cavaliere, Jérôme Chèze, Claudio Chiarabba, John Clinton, Glenn Cougoulat, Wayne C. Crawford, Luigia Cristiano, Tibor Czifra, Ezio D'Alema, Stefania Danesi, Romuald Daniel, Anke Dannowski, Iva Dasović, Anne Deschamps, Jean-Xavier Dessa, Cécile Doubre, Sven Egdorf, Ethz-Sed Electronics Lab, Tomislav Fiket, Kasper Fischer, Wolfgang Friederich, Florian Fuchs, Sigward Funke, Domenico Giardini, Aladino Govoni, Zoltán Gráczer, Gidera Gröschl, Stefan Heimers, Ben Heit, Davorka Herak, Marijan Herak, Johann Huber, Dejan Jarić, Petr Jedlička, Yan Jia, Hélène Jund, Edi Kissling, Stefan Klingen, Bernhard Klotz, Petr Kolínský, Heidrun Kopp, Michael Korn, Josef Kotek, Lothar Kühne, Krešo Kuk, Dietrich Lange, Jürgen Loos, Sara Lovati, Deny Malengros, Lucia Margheriti, Christophe Maron, Xavier Martin, Marco Massa, Francesco Mazzarini, Thomas Meier, Laurent Métral, Irene Molinari, Milena Moretti, Anna Nardi, Jurij Pahor, Anne Paul, Catherine Péquegnat, Daniel Petersen, Damiano Pesaresi, Davide Piccinini, Claudia Piromallo, Thomas Plenefisch, Jaroslava Plomerová, Silvia Pondrelli, Snježan Prevolnik, Roman Racine, Marc Régnier, Miriam Reiss, Joachim Ritter, Georg Rümpker, Simone Salimbeni, Marco Santulin, Werner Scherer, Sven Schippkus, Detlef Schulte-Kortnack, Vesna Šipka, Stefano Solarino, Daniele Spallarossa, Kathrin Spieker, Josip Stipčević, Angelo Strollo, Bálint Süle, Gyöngyvér Szanyi, Eszter Szűcs, Christine Thomas, Martin Thorwart, Frederik Tilmann, Stefan Ueding, Massimiliano Vallocchia, Luděk Vecsey, René Voigt, Joachim Wassermann, Zoltán Wéber, Christian Weidle, Viktor Wesztergom, Gauthier Weyland, Stefan Wiemer, Felix Wolf, David Wolyniec, Thomas Zieke, Mladen Živčić, Helena Žlebčíková.

REFERENCES

Agius, M.R. & Lebedev, S., 2013. Tibetan and Indian lithospheres in the upper mantle beneath Tibet: evidence from broadband surface-wave dispersion, *Geochem. Geophys. Geosyst.,* **14,** 4260–4281.

Bartzsch, S., Lebedev, S. & Meier, T., 2011. Resolving the lithosphere–asthenosphere boundary with seismic Rayleigh waves, *Geophys. J. Int.,* **186**(3), 1152–1164.

Baumont, D., Paul, A., Zandt, G., Beck, S.L. & Pedersen, H.A., 2002. Lithospheric structure of the central Andes based on surface wave dispersion, *J. geophys. Res.,* **107,** doi:10.1029/2001JB000345.

Beucler, É., Stutzmann, É. & Montagner, J.-P., 2003. Surface wave higher-mode phase velocity measurements using a roller-coaster-type algorithm, *Geophys. J. Int.,* **155,** 289–307.

Beyreuther, M., Barsch, R., Krischer, L., Megies, T., Behr, Y. & Wassermann, J., 2010. ObsPy: a python toolbox for seismology, *Seismol. Res. Lett.,* **81**(3), 530–533.

Bodin, T. & Maupin, V., 2008. Resolution potential of surface wave phase velocity measurements at small arrays, *Geophys. J. Int.,* **172,** 698–706.

Bourova, E., Kassaras, I., Pedersen, H.A., Yanovskaya, T., Hatzfeld, D. & Kiratzi, A., 2005. Constraints on absolute S velocities beneath the Aegean Sea from surface wave analysis, *Geophys. J. Int.,* **160,** 1006–1019.

Brokešová, J. & Málek, J., 2016. Small-aperture-array translational and rotational seismograms from distant sources – an example of the Jan Mayen Mw 6.8 of 30 August 2012 earthquake, *Phys. Earth planet. Inter.,* **256,** 1–12.

Brokešová, J. & Málek, J., 2018. Small-aperture seismic array data processing using a representation of seismograms at zero-crossing points, *Phys. Earth planet. Inter.,* **280,** 53–68.

Brune, J.N., Nafe, J.E. & Oliver, J.E., 1960. A simplified method for the analysis and synthesis of dispersed wave trains, *J. geophys. Res.,* **65,** 287–303.

Brune, J.N., Benioff, H. & Ewing, M., 1961. Long-period surface waves from the Chilean earthquake of May 22, 1960, recorded on linear strain seismographs, *J. geophys. Res.,* **66,** 2895–2910.

Brune, J. & Dorman, J., 1963. Seismic waves and earth structure in the Canadian shield, *Bull. seism. Soc. Am.,* **53**(1), 167–209.

Bruneton, M. *et al.*, 2004. Complex lithospheric structure under the central Baltic Shield from surface wave tomography, *J. geophys. Res.,* **109,** B10303, doi:10.1029/2003JB002947.

BW - Department Of Earth And Environmental Sciences, Geophysical Observatory, University Of Munchen, 2001. BayernNetz [Data set], International Federation of Digital Seismograph Networks, https://doi.org/10.7914/SN/BW.

Capon, J., 1970. Analysis of Rayleigh-wave multipath propagation at LASA, *Bull. seism. Soc. Am.,* **60**(5), 1701–1731.

Cara, M., 1979. Lateral variations of S velocity in the upper mantle from higher Rayleigh modes, *Geophys. J. R. astr. Soc.,* **57,** 649–670.

Carder, D.S., 1934. Seismic surface waves and the crustal structure of the Pacific region, *Bull. seism. Soc. Am.,* **24**(3), 231–302.

CH - Swiss Seismological Service (SED) At ETH Zurich, 1983. *National Seismic Networks of Switzerland*. ETH Zürich. https://doi.org/10.12686/sed/networks/ch.

Cotte, N., Pedersen, H.A., Campillo, M., Farra, V. & Cansi, Y., 2000. Off-great-circle propagation of intermediate-period surface waves observed on a dense array in the French Alps, *Geophys. J. Int.,* **142,** 825–840.

Cotte, N., Pedersen, H.A. & TOR Working Group, 2002. Sharp contrast in lithospheric structure across the Sorgenfrei–Tornquist Zone as inferred by Rayleigh wave analysis of TOR1 project data, *Tectonophysics,* **360,** 75–88, doi:10.1016/S0040-1951(02)00348-7.

CR - University Of Zagreb, 2001. Croatian Seismograph Network [Data set], International Federation of Digital Seismograph Networks. Available from: https://doi.org/10.7914/SN/CR.

CZ - Institute Of Geophysics, Academy of Sciences of the Czech Republic, 1973. *Czech Regional Seismic Network*. International Federation of Digital Seismograph Networks.https://doi.org/10.7914/SN/CZ.

Darbyshire, F.A., Larsen, T.B., Mosegaard, K., Dahl-Jensen, T., Gudmundsson, Ó., Bach, T., Gregersen, S., Pedersen, H.A. & Hanka, W., 2004. A first detailed look at the Greenland lithosphere and upper mantle, using Rayleigh wave tomography, *Geophys. J. Int.,* **158,** 267–286.

Darbyshire, F.A. & Lebedev, S., 2009. Rayleigh wave phase-velocity heterogeneity and multilayered azimuthal anisotropy of the Superior Craton, Ontario, *Geophys. J. Int.,* **176,** 215–234.

Dean, E.A., 1986. The simultaneous smoothing of phase and group velocities from multi-event surface wave data, *Bull. seism. Soc. Am.,* **76**(5), 1367–1383.

De Barros, L., Pedersen, H.A., Métaxian, J.-P., Valdés-Gonzalez, C. & Lesage, P., 2008. Crustal structure below Popocatépetl Volcano (Mexico) from analysis of Rayleigh waves, *J. Volc. Geotherm. Res.,* **170**(1–2), 5–11.

de Vos, D., Paulssen, H. & Fichtner, A., 2013. Finite-frequency sensitivity kernels for two-station surface wave measurements, *Geophys. J. Int.,* **194,** 1042–1049.

Debayle, E., Dubuffet, F. & Durand, S., 2016. An automatically updated S-wave model of the upper mantle and the depth extent of azimuthal anisotropy, *Geophys. Res. Lett.,* **43,** 674–682.

Dziewonski, A.M., 1970. On regional differences in dispersion of mantle Rayleigh waves, *Geophys. J. Int.,* **22,** 289–325.

Dziewonski, A. & Landisman, M., 1970. Great circle Rayleigh and Love wave dispersion from 100 to 900 seconds, *Geophys. J. Int.,* **19,** 37–91.

Dziewonski, A.M. & Anderson, D.L., 1981. Preliminary reference Earth model, *Phys. Earth planet. Inter.,* **25**(4), 297–356.

Ekström, G., 2014. Love and Rayleigh phase-velocity maps, 5–40 s, of the western and central USA from USArray data, *Earth planet. Sci. Lett.,* **402,** 42–49.

Evernden, J.F., 1954. Direction of approach of Rayleigh waves and related problems (Part II), *Bull. seism. Soc. Am.,* **44**(2A), 159–184.

Ferreira, A.M.G. & Woodhouse, J.H., 2007. Source, path and receiver effects on seismic surface waves, *Geophys. J. Int.,* **168,** 109–132.

Forsyth, D.W. & Li, A., 2005. Array analysis of two-dimensional variations in surface wave phase velocity and azimuthal anisotropy in the presence of multipathing interference, in *Seismic Earth: Array Analysis of Broadband Seismograms,* Geophys. Monogr. Ser., Vol. **157,** pp. 81–97, eds., Levander, A. & Nolet, G.. doi:10.1029/157GM06.

Foster, A., Ekström, G. & Hjörleifsdóttir, V., 2014. Arrival-angle anomalies across the USArray Transportable Array, *Earth planet. Sci. Lett.,* **402,** 58–68.

FR - RESIF, 1995. *RESIF-RLBP French Broad-band network, RESIF-RAP strong motion network and other seismic stations in metropolitan France [Data set]*. RESIF - Réseau Sismologique et géodésique Français. https://doi.org/10.15778/RESIF.FR.

Friederich, W., 1998. Wave-theoretical inversion of teleseismic surface waves in a regional network: phase-velocity maps and a three-dimensional upper-mantle shear-wave-velocity model for southern Germany, *Geophys. J. Int.,* **132,** 203–225.

Fuchs, F., Kolínský, P., Gröschl, G., Apoloner, M.-T., Qorbani, E., Schneider, F. & Bokelmann, G., 2015. Site selection for a countrywide temporary network in Austria: noise analysis and preliminary performance, *Adv. Geosci.,* **41,** 25–33.

Fuchs, F., Kolínský, P., Gröschl, G., Bokelmann, G. & the AlpArray Working Group, 2016. AlpArray in Austria and Slovakia: technical realization, site description and noise characterization, *Adv. Geosci.,* **43,** 1–13.

G - Institut De Physique Du Globe De Paris (IPGP), & Ecole Et Observatoire Des Sciences De La Terre De Strasbourg (EOST), 1982. *GEOSCOPE, French Global Network of broad band seismic stations*. Institut de Physique du Globe de Paris (IPGP). https://doi.org/10.18715/GEOSCOPE.G.

GE - GEOFON Data Centre, 1993. *GEOFON Seismic Network*. Deutsches GeoForschungsZentrum GFZ. https://doi.org/10.14470/TR560404.

GR - Federal Institute for Geosciences and Natural Resources (BGR), 1976. *German Regional Seismic Network (GRSN)*. Federal Institute for Geosciences and Natural Resources (BGR). https://doi.org/10.25928/mbx6-hr74.

GU - University Of Genova, 1967. *Regional Seismic Network of North Western Italy*. International Federation of Digital Seismograph Networks. https://doi.org/10.7914/SN/GU.

Gupta, H.K., Nyman, D.C. & Landisman, M., 1977. Shield-like upper mantle structure inferred from long-period Rayleigh- and Love-wave dispersion investigations in the Middle East and Southeast Asia, *Bull. seism. Soc. Am.,* **67**(1), 103–119.

Harkrider, D.G. & Anderson, D.L., 1962. Computation of surface wave dispersion for multilayered aniostropic media, *Bull. seism. Soc. Am.,* **52**(2), 321–332.

Harkrider, D.G., 1970. Surface waves in multilayered elastic media. Part II. Higher mode spectra and spectral ratios from point sources in plane layered Earth models, *Bull. seism. Soc. Am.,* **60**(6), 1937–1987.

Hetényi, G. *et al.*, 2018, The AlpArray Seismic network: a large-scale european experiment to image the Alpine Orogen, *Surv. Geophys.,* **39,** 1009–1033.

HU - Kövesligethy Radó Seismological Observatory (Geodetic And Geophysical Institute, Research Centre For Astronomy And Earth Sciences, Hungarian Academy Of Sciences (MTA CSFK GGI KRSZO)), 1992. *Hungarian National Seismological Network*. Deutsches GeoForschungsZentrum GFZ. https://doi.org/10.14470/UH028726.

Hwang, R.-D. & Yu, G.-K., 2005. Shear-wave velocity structure of upper mantle under Taiwan from the array analysis of surface waves, *Geophys. Res. Lett.,* **32,** L07310, doi: 10.1029/2004GL021868.

Isse, T., Suetsugu, D., Shiobara, H., Fukao, Y., Mochizuki, K., Kanazawa, T., Sugioka, H., Kodaira, S. & Hino, R., 2003. Rayleigh wave phase velocities beneath the northeastern Philippine Sea as determined by data from long term broadband ocean bottom seismographs, *Frontier Research on Earth Evolution, IFREE Report for 2001–2002,* Vol. **1,** pp. 31–35.

IV - INGV Seismological Data Centre, 2006. *Rete Sismica Nazionale (RSN)*. Istituto Nazionale di Geofisica e Vulcanologia (INGV), Italy. https://doi.org/10.13127/SD/X0FXnH7QfY.

James, E.K., Dalton, C.A. & Gaherty, J.B., 2014. Rayleigh wave phase velocities in the Atlantic upper mantle, *Geochem. Geophys. Geosyst.,* **15,** 4305–4324.

Kaviani, A., Paul, A., Bourova, E., Hatzfeld, D., Pedersen, H. & Mokhtari, M., 2007. A strong seismic velocity contrast in the shallow mantle across the Zagros collision zone (Iran), *Geophys. J. Int.,* **171**(1), 399–410.

Knopoff, L., Mueller, S. & Pilant, W.L., 1966. Structure of the crust and upper mantle in the ALPS from the phase velocity of Rayleigh waves, *Bull. seism. Soc. Am.,* **56**(5), 1009–1044.

Knopoff, L. & Mal, A.K., 1967. Phase velocity of surface waves in the transition zone of continental margins: 1. Love waves, *J. geophys. Res.,* **72**(6), 1769–1776.

Knopoff, L., Berry, M.J. & Schwab, F.A., 1967. Tripartite phase velocity observations in laterally heterogeneous regions, *J. geophys. Res.,* **72**(10), 2595–2601.

Knopoff, L., Schlue, J.W. & Schwab, F.A., 1970. Phase velocities of Rayleigh waves across the East Pacific Rise, *Tectonophysics,* **10**(1–3), 321–334.

Knopoff, L., 1972. Observation and inversion of surface-wave dispersion in A.R. Ritsema (Editor), The Upper Mantle, *Tectonophysics,* **13**(1–4), 497–519.

Kolínský, P. & Brokešová, J., 2007. The Western Bohemia uppermost crust shear wave velocities from Love wave dispersion, *J. Seismol.,* **11,** 101–120.

Kolínský, P., Málek, J. & Brokešová, J., 2011. Shear wave crustal velocity model of the western Bohemian Massif from Love wave phase velocity dispersion, *J. Seismol.,* **15,** 81–104.

Kolínský, P., Valenta, J. & Málek, J., 2014. Velocity model of the Hronov-Poříčí Fault Zone from Rayleigh wave dispersion, *J. Seismol.,* **18,** 617–635.

Kolínský, P., Bokelmann, G. & the AlpArray Working Group, 2019. Arrival angles of teleseismic fundamental mode Rayleigh waves across the AlpArray, *Geophys. J. Int.,* **218,** 114–144.

Kolínský, P., Schneider, F.M. & Bokelmann, G., 2020. Surface wave diffraction pattern recorded on AlpArray: Cameroon Volcanic Line case study, *J. geophys. Res: Solid Earth,* **125,** e2019JB019102, doi:10.1029/2019JB019102.

Köhler, A., Maupin, V. & Balling, N., 2015. Surface wave tomography across the Sorgenfrei–Tornquist Zone, SW Scandinavia, using ambient noise and earthquake data, *Geophys. J. Int.,* **203,** 284–311.

LC - Laboratorio Subterraneo De Canfranc, 2011. *LSC (Laboratorio Subterraneo Canfranc)*. International Federation of Digital Seismograph Networks. https://doi.org/10.7914/SN/LC.

Lebedev, S., Adam, J.M.-C. & Meier, T., 2013. Mapping the Moho with seismic surface waves: A review, resolution analysis, and recommended inversion strategies, *Tectonophysics,* **609,** 377–394.

Legendre, C.P., Deschamps, F., Zhao, L., Lebedev, S. & Chen, Q.-F., 2014. Anisotropic Rayleigh wave phase velocity maps of eastern China, *J. geophys. Res. Solid Earth,* **119,** 4802–4820.

Levshin, A.L., Ratnikova, L. & Berger, J., 1992. Peculiarities of surface-wave propagation across central Eurasia, *Bull. seism. Soc. Am.,* **82**(6), 2464–2493.

Li, Y., Wu, Q., Pan, J. & Sun, L., 2012. S-wave velocity structure of northeastern China from joint inversion of Rayleigh wave phase and group velocities, *Geophys. J. Int.,* **190,** 105–115.

Liu, Y. & Holt, W.E., 2015. Wave gradiometry and its link with Helmholtz equation solutions applied to USArray in the eastern U.S., *J. geophys. Res.,* **120,** 5717–5746.

Love, A.E.H., 1911. *Some Problems of Geodynamics,* Cambridge Univ. Press, 180pp.

Luo, Y., Yang, Y., Zhao, K., Xu, Y. & Xia, J., 2015. Unraveling overtone interferences in Love-wave phase velocity measurements by radon transform, *Geophys. J. Int.,* **203,** 327–333.

Lyu, Ch., Pedersen, H.A., Paul, A., Zhao, L., Solarino, S. & CIFALPS Working Group, 2017. Shear wave velocities in the upper mantle of the Western Alps: new constraints using array analysis of seismic surface waves, *Geophys. J. Int.,* **210,** 321–331.

Magrini, F., Diaferia, G., Boschi, L. & Cammarano, F., 2020. Arrival-angle effects on two-receiver measurements of phase velocity, *Geophys. J. Int.,* **220,** 1838–1844.

Maupin, V., 2011. Upper-mantle structure in southern Norway from beamforming of Rayleigh wave data presenting multipathing, *Geophys. J. Int.,* **185,** 985–1002.

McEvilly, T.V., 1964. Central U.S. crust – upper mantle structure from Love and Rayleigh wave phase velocity inversion, *Bull. seism. Soc. Am.,* **54**(6A), 1997–2015.

Meier, T., Dietrich, K., Stöckhert, B. & Harjes, H.-P., 2004. One-dimensional models of shear wave velocity for the eastern Mediterranean obtained from the inversion of Rayleigh wave phase velocities and tectonic implications, *Geophys. J. Int.,* **156,** 45–58.

Mitra, S., Priestley, K., Gaur, V.K. & Rai, S.S., 2006. Shear-wave structure of the South Indian lithosphere from Rayleigh wave phase-velocity measurements, *Bull. seism. Soc. Am.,* **96**(4A), 1551–1559.

MN - MedNet Project Partner Institutions, 1990. *Mediterranean Very Broadband Seismographic Network (MedNet)*. Istituto Nazionale di Geofisica e Vulcanologia (INGV). https://doi.org/10.13127/SD/fBBBtDtd6q.

MT - French Landslide Observatory – Seismological Datacenter / RESIF. 2006. *Observatoire Multi-disciplinaire des Instabilités de Versants (OMIV) [Data set]*. RESIF - Réseau Sismologique et géodésique Français. https://doi.org/10.15778/RESIF.MT.

Nishimura, C.E. & Forsyth, D.W., 1989. The anisotropic structure of the upper mantle in the Pacific, *Geophys. J. Int.,* **96**(2), 203–229.

Nolet, G. & Dahlen, F.A., 2000. Wave front healing and the evolution of seismic delay times, *J. geophys. Res.,* **105**(B8), 19,043–019,054.

Noponen, I., 1966. Surface wave phase velocities in Finland, *Bull. seism. Soc. Am.,* **56**(5), 1093–1104.

Novotný, O., 1970. Partial derivatives of dispersion curves of Love waves in a layered medium, *Stud. Geophys. Geod.,* **14,** 36–50.

Novotný, O. & Vaněk, J., 1983. Theoretical dispersion curves for the seismic profile Kašperské Hory (Czechoslovakia) – Ksiaz (Poland), *Stud. Geophys. Geod.,* **27,** 157–163.

Novotný, O., Mufti, I. & Vicentini, A.G., 2005. Analytical partial derivatives of the phase- and group velocities for Rayleigh waves propagating in a layer on a half-space, *Stud. Geophys. Geod.,* **49,** 305–321.

O'Donnell, J.P., Adams, A., Nyblade, A.A., Mulibo, G.D. & Tugume, F., 2013. The uppermost mantle shear wave velocity structure of eastern Africa from Rayleigh wave tomography: constraints on rift evolution, *Geophys. J. Int.,* **194,** 961–978.

OE – ZAMG - Zentralanstalt Für Meterologie Und Geodynamik, 1987. *Austrian Seismic Network*. International Federation of Digital Seismograph Networks. https://doi.org/10.7914/SN/OE.

Oldham, R.D., 1900. On the propagation of earthquake motion to great distances, *Phil. Trans. R. Soc. Lond., A,* **194,** 135–174.

Oliver, J., 1962. A summary of observed seismic surface wave dispersion, *Bull. seism. Soc. Am.,* **52**(1), 81–86.

OT - University Of Bari "Aldo Moro", 2013. *OTRIONS, Seismic networks of Gargano Area (Italy)*. International Federation of Digital Seismograph Networks. https://doi.org/10.7914/SN/OT.

OX - OGS (Istituto Nazionale Di Oceanografia E Di Geofisica Sperimentale), 2016. *North-East Italy Seismic Network*. International Federation of Digital Seismograph Networks. https://doi.org/10.7914/SN/OX.

Palomeras, I., Thurner, S., Levander, A., Liu, K., Villasenor, A., Carbonell, R. & Harnafi, M., 2014. Finite-frequency Rayleigh wave tomography of the western Mediterranean: Mapping its lithospheric structure, *Geochem. Geophys. Geosyst.,* **15,** 140–160.

Patton, H., 1980. Crust and upper mantle structure of the Eurasian continent from the phase velocity and Q of surface waves, *Rev. Geophys.,* **18**(3), 605–625.

Pedersen, H.A., Coutant, O., Deschamps, A., Soulage, M. & Cotte, N., 2003. Measuring surface wave phase velocities beneath small broad-band arrays: tests of an improved algorithm and application to the French Alps, *Geophys. J. Int.,* **154,** 903–912.

Pedersen, H.A., 2006. Impacts of non-plane waves on two-station measurements of phase velocities, *Geophys. J. Int.,* **165,** 279–287.

Pedersen, H.A., Bruneton, M., Maupin, V. &SVEKALAPKO Seismic Tomography Working Group, 2006: Lithospheric and sublithospheric anisotropy beneath the Baltic shield from surface-wave array analysis, *Earth planet. Sci. Lett.,* **244,** 590–605.

Pedersen, H.A., Debayle, E., Maupin, V. & the POLENET/LAPNET Working Group, 2013. Strong lateral variations of lithospheric mantle beneath cratons – Example from the Baltic Shield, *Earth planet. Sci. Lett.,* **383,** 164–172.

Pedersen, H.A., Boué, P., Poli, P. & Colombi, A., 2015. Arrival angle anomalies of Rayleigh waves observed at a broadband array: a systematic study based on earthquake data, full waveform simulations and noise correlations, *Geophys. J. Int.,* **203,** 1626–1641.

Pilant, W.L. & Knopoff, L., 1964. Observations of multiple seismic events, *Bull. seism. Soc. Am.,* **54**(1), 19–39.

Plešinger, A., Neunhöfer, H. & Wielandt, E., 1991. Crust and upper mantle structure of the Bohemian Massif from the dispersion of seismic surface waves, *Stud. Geophys. Geod.,* **35,** 184–195.

Polat, G., Lebedev, S., Readman, P.W., O'Reilly, B.M. & Hauser, F., 2012. Anisotropic Rayleigh-wave tomography of Ireland's crust: Implications for crustal accretion and evolution within the Caledonian Orogen, *Geophys. Res. Lett.,* **39,** L04302, doi:10.1029/2012GL051014.

Press, F., 1956. Determination of crustal structure from phase velocity of Rayleigh waves. Part I: Southern California, *Bull. geol. Soc. Am.,* **67**(12), 1647–1658.

Press, F., 1957. Determination of crustal structure from phase velocity of Rayleigh waves. Part II: San Francisco Bay region, *Bull. seism. Soc. Am.,* **47**(2), 87–88.

Priestley, K. & Brune, J., 1978. Surface waves and the structure of the Great Basin of Nevada and western Utah, *J. geophys. Res.,* **83**(B5), doi:10.1029/JB083iB05p02265.

Prindle, K. & Tanimoto, T., 2006. Teleseismic surface wave study for S-wave velocity structure under an array: Southern California, *Geophys. J. Int.,* **166,** 601–621.

Pyle, M.L., Wiens, D.A., Weeraratne, D.S., Shore, P.J., Shiobara, H. & Sugioka, H., 2010. Shear velocity structure of the Mariana mantle wedge from Rayleigh wave phase velocities, *J. geophys. Res.,* **115,** B11304, doi: 10.1029/2009JB006976.

Rayleigh, J.W.S., 1885. On waves propagating along the plane surface of an elastic solid, *Proc. Lond. Math. Soc.,* **17,** 4–11.

RD - RESIF, 2018. *CEA/DASE broad-band permanent network in metropolitan France [Data set]*. RESIF - Réseau Sismologique et géodésique Français. https://doi.org/10.15778/RESIF.RD.

Romanowicz, B.A., 1982. Constraints on the structure of the Tibet Plateau from pure path phase velocities of Love and Rayleigh waves, *J. geophys. Res.,* **87**(B8), 6865–6883, doi:10.1029/JB087iB08p06865.

Salaün, G., Pedersen, H.A., Paul, A., Farra, V., Karabulut, H., Hatzfeld, D., Papazachos, C., Childs, D.M. & Pequegnat, C. SIMBAAD Team, 2012. High resolution surface wave tomography beneath the Aegean-Anatolia region: constraints on upper-mantle structure, *Geophys. J. Int.,* **190,** 406–420.

Schaeffer, A.J. & Lebedev, S., 2013. Global shear speed structure of the upper mantle and transition zone, *Geophys. J. Int.,* **194**(1), 417–449.

SK - ESI SAS (Earth Science Institute Of The Slovak Academy Of Sciences), 2004. *National Network of Seismic Stations of Slovakia*. Deutsches GeoForschungsZentrum GFZ. https://doi.org/10.14470/FX099882.

SL - Slovenian Environment Agency, 2001. *Seismic Network of the Republic of Slovenia*. International Federation of Digital Seismograph Networks. https://doi.org/10.7914/SN/SL.

Smith, D.B., Ritzwoller, M.H. & Shapiro, N.M., 2004. Stratification of anisotropy in the Pacific upper mantle, *J. geophys. Res.,* **109,** B11309, doi:10.1029/2004JB003200.

Soomro, R.A., Weidle, C., Cristiano, L., Lebedev, S., Meier, T. & PASSEQ Working Group, 2016. Phase velocities of Rayleigh and Love waves in central and northern Europe from automated, broad-band, interstation measurements, *Geophys. J. Int.,* **204,** 517–534.

ST - Geological Survey-Provincia Autonoma Di Trento, 1981. *Trentino Seismic Network*. International Federation of Digital Seismograph Networks. https://doi.org/10.7914/SN/ST.

Stange, S. & Friederich, W., 1993. Surface wave dispersion and upper mantle structure beneath southern Germany from joint inversion of network recorded teleseismic events, *Geoph. Res. Lett.,* **20,** 2375–2378.

SX - Leipzig University. 2001. *SXNET Saxon Seismic Network*. International Federation of Digital Seismograph Networks. https://doi.org/10.7914/SN/SX.

TH - Jena, F. S. U., 2009. *Thüringer Seismologisches Netz (TSN)*. International Federation of Digital Seismograph Networks. https://doi.org/10.7914/SN/TH.

Thatcher, W. & Brune, J.N., 1969. Higher mode interference and observed anomalous apparent Love wave phase velocities, *J. geophys. Res.,* **74,** 6603–6611.

Villaseñor, A., Ritzwoller, M.H., Levshin, A.L., Barmin, M.P., Engdahl, E.R., Spakman, W. & Trampert, J., 2001. Shear velocity structure of Central Eurasia from inversion of surface wave velocities, *Phys. Earth planet. Inter.,* **123,** 169–184.

Weidner, D.J., 1972. Rayleigh waves from mid-ocean ridge earthquakes: source and path effects, *PhD thesis,* Massachusetts Institute of Technology, Dept. of Earth and Planetary Science, 1972.

Weidner, D.J., 1974. Rayleigh wave phase velocities in the Atlantic Ocean, *Geophys. J. Int.,* **36**(1), 105–139.

Wessel, P., Smith, W.H.F., Scharroo, R., Luis, J. & Wobbe, F., 2013. Generic Mapping Tools: improved version released, *EOS, Trans. Am. geophys. Un.,* **94**(45), 409–410.

Widmer-Schnidrig, R. & Laske, G., 2007. Theory and observations – normal modes and surface wave measurements, in Seismology and structure of the Earth, vol. **1,** In: Romanowicz, B.A., Dziewonski, A.M. & Schubert, G., editors. *Treatise on Geophysics,* pp. 67–125, Elsevier, doi:10.1016/B978-044452748-6.00003-1.

Wielandt, E., 1993. Propagation and structural interpretation of non-plane waves, *Geophys. J. Int.,* **113**(1), 45–53.

Wilson, J.T., 1940. The Love waves of the South Atlantic earthquake of August 28, 1933, *Bull. seism. Soc. Am.,* **30**(3), 273–301.

Wilson, J.T. & Baykal, O., 1948. Crustal structure of the North Atlantic Basin as determined from Rayleigh-wave dispersion, *Bull. seism. Soc. Am.,* **38**(1), 41–53.

Wu, T, Zhang, S., Cao, Z., Li, M., Hua, Y., Fu, X. & Wei, Y., 2020. Lithospheric structure of Hubei Province, central China, from Rayleigh wave tomography: insight into the spatial contact relationship between the Yangtze Plate and the eastern Qinling-Dabie orogenic belt, *Geophys. J. Int.,* **221,** 1669–1683.

Yoshida, Y. & Suetsugu, D., 2004. Lithospheric thickness beneath the Pitcairn hot spot trail as inferred from Rayleigh wave dispersion, *Phys. Earth planet. Inter.,* **146,** 75–85.

Yoshizawa, K. & Kennett, B.L.N., 2004. Multimode surface wave tomography for the Australian region using a three-stage approach incorporating finite frequency effects, *J. geophys. Res.,* **109,** doi:10.1029/2002JB002254.

Z3 - AlpArray Seismic Network, 2015. *AlpArray Seismic Network (AASN) temporary component*. AlpArray Working Group. https://doi.org/10.12686/alparray/z3_2015.

Zhai, Q., Yao, H. & Peng, Z., 2019. Upper-mantle shear velocity structure beneath the equatorial East Pacific Rise from array-based teleseismic surface wave dispersion analysis, *Geophys. J. Int.,* **219,** 607–618.

APPENDIX: OVERVIEW OF DISPERSION-CURVE MEASUREMENT

In the Introduction section, we mentioned the most important papers regarding the main topics in development of the phase-velocity measurement. Here, in the Appendix, we extend the overview to more papers, commenting them as well as those mentioned already in the Introduction and discussing, how they are related to our current work. The Appendix follows the structure of the Introduction, repeating the most important ideas and enriching them with details. There are hundreds of papers on the surface wave propagation topic. We mention those showing and commenting phase-velocity dispersion curves. An overview of literature about peculiarities of surface wave propagation in general is given in the Introduction to the KB2019 paper, where tens of additional references can be found.

A1 Phase-velocity dispersion curves

Although Rayleigh (1885) predicted the surface waves without a need of dispersion using only a half-space, Oldham (1900) already noted that the observed velocity of the waves depends on their 'size' with bigger waves propagating faster. Love (1911) precisely defined the dispersion, even using just one layer over the half-space and saying that both surface-wave types (Rayleigh and Love) propagate faster for longer waves. For Love waves, this holds true for arbitrary number of layers with any properties (any structure): the phase velocity of Love waves always monotonically increases with period. For Rayleigh waves, the situation is more complicated. In certain cases - like for the oceanic lithosphere (e.g. Cara 1979; James *et al.* 2014) - the phase velocity of Rayleigh waves can have a local minimum. Comparison of oceanic Love and Rayleigh wave phase velocities is given by Nishimura & Forsyth (1989). Love waves have monotonically increasing dispersion curves even in the oceans. Nevertheless, also Rayleigh wave phase-velocity dispersion curves are always smooth, generally increasing with period with - at the most complicated case - one minimum spanning a broad range from 30 to 70 s. Wilson (1940) summarized several previous works and supported the theory by observing and modelling group velocities of Love waves propagating from the earthquake in the South Atlantic ocean. Press (1956) added models of phase velocities for Rayleigh waves in Southern California with monotonous dispersion curves. Oliver (1962) summarized the knowledge showing modelled group- and phase-velocity dispersion curves for both Love and Rayleigh waves.

A2 Early phase-velocity observations

Since then, the theory holds true, however, it is somewhat in contrast with the observation. Evernden (1954) measured Rayleigh wave phase velocities using the tripartite method in the San Francisco Bay. The dispersion curve he presented is composed of separated values, however, it shows non-random fluctuations. The same data was later processed by Press (1957). Brune & Dorman (1963) used a technique for measuring phase velocities, which later become known as the 'two-station' method. The measured phase-velocity dispersion curves for both Love and Rayleigh waves in the Canadian shield show a significant 'scatter', as the authors called the apparently random deviations of velocities for a given path. McEvilly (1964) compared the tripartite method with the two-station method. As the tripartite method produced significant scatter, he concluded that the two-station method is more suitable for phase-velocity measurements. This is an interesting conclusion, because the tripartite method can be considered as a predecessor of array techniques, which are considered superior to the two-station method nowadays. In this paper, however, we have shown, why array measurements are affected by the dynamic effects and that the bias is almost the same as for the two-station measurement. As both latter studies showed only sparse measurement in terms of periods, the scatter of the values seemed to be random. Pilant & Knopoff (1964) already noted that if two or more wave trains interfere, not only the amplitude shows beats, but also the phases are affected by 'fluctuations'. Their examples of dispersion curves are again given by scattered points only, however, we can very clearly see the observed phase velocity varying around the smooth monotonic modelled curves. Knopoff *et al.* (1966) continued in this work showing many other examples of dispersion curves affected by 'phase irregularities' and hence yielding fluctuations. He also noted that these phase irregularities made it almost impossible to compute a structure from the observation. One of the best examples of dispersion curves affected by fluctuations is given by Noponen (1966) who studied propagation of surface waves from earthquakes in Greece through the Baltic Shield, see Fig. 1 of our current paper. He concluded that these 'disturbances' or 'oscillations' cannot be real variations in velocity because of their rapid changes and because they were smaller on longer paths. His observation fits exactly to what we observe and explain today. Dziewonski & Landisman (1970) discussed 'small changes in the derivative of the phase-velocity curve' showing examples of long-period (over 100 s) world-circling surface waves. Many examples of dispersion curves with 'irregularities' (or 'fluctuations', or 'oscillating phase-velocity curves') were given by Weidner (1974) for paths crossing the Atlantic Ocean.

Important to note is that all the above mentioned authors recognized that the measurement could not be explained by structural models. Some of them already excluded the measurement errors as a cause.

A3 Recent observations

Looking at papers published several decades later, we see that little has changed. Plešinger *et al.* (1991) measured both Love and Rayleigh wave dispersion using the two-station method across the Bohemian Massif. Both types of dispersion show wobbled character. Isse *et al.* (2003) used the two-station method for measurement of Rayleigh waves crossing the Philippine Sea. Their single-path dispersion curves show again similar wobbles. Pedersen *et al.* (2003) used the two-station method for the French Alps showing figures with dispersion affected by the wobbles as well. Yoshida & Suetsugu (2004) obtained wobbled dispersion curves for oceanic paths. Meier *et al.* (2004) presented wobbled dispersion curves for the Mediterranean region, Kolínský *et al.* (2011) showed the same for the Bohemian Massif (talking about 'undulations'). Other examples, among many others, are Polat *et al.* (2012) showing examples

of dispersion curves measured for the surface-wave tomography of Ireland and Agius & Lebedev (2013) using the two-station method in Tibet. Pedersen *et al.* (2015) showed, in addition, similar wobbles in backazimuths of surface wave propagating across the LAPNET network. Somroo *et al.* (2016) measured tens of thousand dispersion curves across Europe and from the examples shown, they suffered by the wobbles as well. Many studies nowadays, however, do not show the dispersion curves in figures any more as the amount of data processed and number of curves measured increases dramatically in surface-wave tomography (Schaeffer & Lebedev 2013; Debayle *et al.* 2016).

Wobbled dispersion curves are unlikely to be associated with any particular measurement method. Brokešová & Málek (2016, 2018) showed wobbled curves measured at a small-aperture array using rotation-to-translation relation applied on earthquake record.

A4 Modelled, long-path and regionalized curves do not have wobbles

Many papers show phase-velocity dispersion curves, which are smooth and simple (monotonic, no wobbles). There are three reasons for the curves to be simple.

Modelled dispersion curves

Phase-velocity dispersion curves calculated from a structural model are always simple (no wobbles). Hundreds of papers show such theoretical dispersion curves. Carder (1934) plotted phase-velocity dispersion curves for Love waves in one layer giving examples for different thicknesses. He pointed out the difference between oceanic and continental propagation and he used the term 'normal dispersion' for longer waves having higher speeds. Theoretical curves for Rayleigh waves were then given by Wilson & Baykal (1948). Evernden (1954) presented theoretical curves for fundamental and higher modes of both Love and Rayleigh waves for both (simple) continental and oceanic models. Simple modelled dispersion curves are then presented in all studies up to now (e.g. Press 1956; Brune *et al.* 1960 and 1961; Harkrider & Anderson 1962; Brune & Dorman 1963; McEvilly 1964; Harkrider 1970; Knopoff 1972; Priestley & Brune 1978; Novotný & Vaněk 1983; Yoshida & Suetsugu 2004; Yoshizawa & Kennett 2004; Ekström 2014; Lyu *et al.* 2017).

Long paths

In addition, there are also measured curves which look quite simple. If we look at curves measured over single paths, meaning between two stations or between the source and a station (single-station method), simple observed curves are always found for long propagation paths (thousands of kilometres, see e.g. Wilson & Baykal 1948; Brune *et al.* 1961; Gupta *et al.* 1977; Romanowicz 1982; Levshin *et al.* 1992; Beucler *et al.* 2003; James *et al.* 2014; and many others). A hint on wobbles being more pronounced when the paths are shorter even when using the same earthquake for the two-station measurement in the same region was already given by Kolínský *et al.* (2011), who measured four short profiles and one long profile crossing the Bohemian Massif.

Regionalized curves

The last category of simple dispersion curves relates again to curves, which are 'observed', however, these are dispersion curves representing not single pure-path measurement, as above, but rather a region or locality. Such dispersion curves can be obtained by averaging or merging the pure-path curves, like by Baumont *et al.* (2002) - network/array analysis and correction of the two-station method, Yoshida & Suetsugu (2004) and references therein, Hwang & Yu (2005) - 1-D array analysis, Agius & Lebedev (2013) - averaging two-station measurements, Palomeras *et al.* (2014) - curves regionalized from tomography and all the other tomographic studies, where the phase-velocity maps are used to compile 'local' dispersion curves characterizing the structure at the given node of the tomography grid. As most of the tomographic papers do not show the local dispersion curves, we mention just a few which do - Villaseñor *et al.* (2001), Bruneton *et al.* (2004), Darbyshire *et al.* (2004), Li *et al.* (2012), Salaün *et al.* (2012), Agius & Lebedev (2013), O'Donnell *et al.* (2013) and Köhler *et al.* (2015). Interestingly, in his review, Patton (1980) presented regionalized curves which still show wobbles. Kolínský *et al.* (2014) obtained slightly wobbled curve when merging only few array measurements and Darbyshire *et al.* (2004) showed little wobbles in local dispersions obtained from tomography. It is possible that if the ray coverage of the tomography is not random and dense enough, the wobbles do not disappear and still affect the tomography results.

Comparison

The difference between the modelled (regionalized, local) and observed pure-path dispersion curves is best-seen in papers which give the direct comparison of both. Starting with the Canadian Shield study by Brune & Dorman (1963), continuing with Priestley & Brune (1978), we can see similar discrepancy between the observed and modelled curves in the recent papers as well (Pyle *et al.* 2010; Bartzsch *et al.* 2011; Kolínský *et al.* 2011, 2014; Palomeras *et al.* 2014; Köhler *et al.* 2015; Brokešová & Málek 2016, 2018).

A5 Possible explanation

Since the first observations, seismologists tried to present an explanation for the discrepancy between simple modelled and wobbled observed curves. Brune & Dorman (1963) attributed the scatter to the interference of Sa and Sn waves with the fundamental modes of surface waves. They concluded that effects of lateral refraction are probably small, however, they noted that lateral refraction may introduce waves coming from different backazimuths. Pilant & Knopoff (1964) described an interference noting that positive and negative fluctuations occur equally. They described fluctuations based on interference from multiple events and signals arriving over multiple paths. They observed that if stations are in different azimuth from the source, or in the same azimuths but different distances, the record spectra differ significantly. Knopoff *et al.* (1966) attributed the complex observation to interference of multipathed wave trains. Knopoff & Mal (1967) described, how the back reflection from inclined Moho produces phase shifts. They modelled successfully a wobbled dispersion. Thatcher & Brune (1969) discussed the mode interference as a possible cause of anomalous apparent phase velocities of Love waves. Since then, the possible explanations repeat regularly in other papers. Dziewonski (1970) - lateral refraction, Capon (1970) - multipathing and refraction at continental margins, Knopoff *et al.* (1970) - scattering effects. A detailed investigation was given by Weidner (1972, 1974): the observed wobbles were attributed to interference caused by waves scattered from the Mid Atlantic Ridge. He suggested that the scattering takes place along the extent of the ridge excluding a single point scattering. He precisely excluded some other possible effects (higher modes, another

earthquake, as suggested earlier, see above). The only option left was that the interfering waves are the same Rayleigh waves, just delayed. His explanation is very close to what we suggest. Already at that time, he was more thinking about the waves being influenced by a phase shift even propagating still as a single wavegroup, which can be seen in contrast to what we nowadays consider as multipathing, where two or more wavegroups are coming to the station as distinct arrivals (Maupin 2011). In principle, it is the same phenomenon, only the time scale differs. Pedersen (2006) studied the effect of noise and non-plane waves on the phase velocities determined by the two-station method. She concluded that these effects diminish for longer profiles. The errors due to the great-circle deviations were, however, independent of profile length. Ferreira & Woodhouse (2007) investigated the influence of source, path and receiver effects on the phase determination concluding that local structure at the receiver is negligible. Phase anomalies were mostly controlled by path effects. Luo *et al*. (2015) removed the interference of higher modes of Love waves, however, even after that, the resulting dispersion still contained wobbles.

A6 How to deal with the wobbles

Together with the attempts of explanation, researchers tried to remove the wobbles. Pilant & Knopoff (1964) used different methods of smoothing taking advantage of the fact that positive and negative fluctuations occurred equally in their observation. McEvilly (1964) assumed a systematic error in the two-station measurement if the waves propagate off the profile path. They decided to favour lower velocities, if the measurement was scattered. Noponen (1966) used smoothing of the phase-velocity wobbles and Dean (1986) suggested simultaneous smoothing of phase and group curves. Similar approach was used also by Mitra *et al.* (2006). Stange & Friederich (1993) inverted simultaneously both amplitude and phase of the wavefield. Darbyshire *et al.* (2004) averaged individual measurement from the two-station method to robust curves representing the interstation profile. This procedure was used as well by Barros *et al.* (2008), Darbyshire & Lebedev (2009) and Legendre *et al.* (2014). Forsyth & Li (2005) proposed the two-plane wave fit to the observe wavefield, what helped to explain the observation better than single-plane assumption. It was later used also by O'Donnell *et al.* (2013). Pedersen *et al.* (2006) determined precisely backazimuths of propagation calculating the mean phase velocity by averaging individual measurements at the SVEKALAPKO array. Similar approach was used also by Pedersen *et al.* (2013). Polat *et al.* (2012) noted that diffraction and interference of the fundamental and higher modes can bias inter-station dispersion measurements. They selected only the smooth portions of the individual dispersion curves and averaged many. Agius & Lebedev (2013) discussed the interference of surface waves with *S* and multiple *S* waves. They found it important especially for Love waves They again used averaging of the individual two-station measurements. Soomro *et al.* (2016) used complex selection of acceptable phase-velocity measurements based on a number of quality criteria including a smoothness requirement. One thing to note here is that all these methods of removing the wobbles are independent of the cause of the wobbles. Averaging and smoothing only removes the wobbles without asking, why they are there. Even the two-plane wave approach is only capable to fit the complex wavefield better than single-plane wave, without explaining, why it is so complex.

A7 Array phase-velocity measurement

It has been repeatedly assumed that array techniques (beamforming) are capable to determine the phase velocity better than the two-station method because it simultaneously searches for both the magnitude of the velocity as well as the direction of propagation (Baumont *et al.* 2002; Bourova *et al.* 2005; Kaviani *et al.* 2007; Barros *et al.* 2008; Lyu *et al.* 2017), summarized by Widmer-Schnidrig & Laske (2007) and references therein. It is true that knowing the arrival angle of incoming waves removes the bias caused by unknown direction of propagation as in the case of the two-station method (e.g. Magrini *et al.* 2020). However, significant wobbles remain at the array-based dispersion curves showing that the non-plane wave character (mentioned by all the papers referenced in the first sentence of this paragraph) causes significantly more serious problem than the unknown arrival angle. Affected dispersion curves were obtained by Press (1956), McEvilly (1964) and Knopoff *et al.* (1967) using the tripartite method (predecessor of array beamforming). Wobbled dispersion curves are shown by Cotte *et al*. (2000, 2002) using array technique, as well as by Pedersen *et al.* (2003) applying beamforming within small arrays and comparing the results with the two-station method. Although the effects of incoming wavefield can be partially suppressed by averaging over many measurements from earthquakes in different backazimuths similarly like in the case of the two-station method, even array-based phase velocities suffer by wobbles. Other examples of such results are given by Hwang & Yu (2005), Kolínský *et al.* (2014), Lyu *et al.* (2017) and Zhai *et al.* (2019). Barros *et al.* (2008) showed that smaller arrays produce higher wobbles than bigger arrays. This effect corresponds to the two-station method also yielding higher wobbles on shorter interstation paths, as we have shown in our study.